Correlation of Damage in Rocks Dynamically Loaded by Percussive Tools Using Piston Coefficient of Restitution (COR)

Jorge Aising, Laurent Gerbaud, Hedi Sellami, Pascale Sénéchal, Peter Moonen

Rock Mechanics and Rock Engineering
https://doi.org/10.1007/s00603-024-04303-9

ORIGINAL PAPER

Correlation of Damage in Rocks Dynamically Loaded by Percussive Tools Using Piston Coefficient of Restitution (COR)

Jorge Aising[1,2] · Laurent Gerbaud[1] · Hedi Sellami[1] · Pascale Sénéchal[3] · Peter Moonen[4]

Received: 6 May 2024 / Accepted: 26 November 2024

Abstract

Efficient drilling operations require optimal drilling parameters to achieve higher penetration rates and minimize tool wear. This study focuses on characterizing the piston coefficient of restitution (COR) as a damage indicator for rocks dynamically loaded by percussive tools. The COR offers a nuanced understanding of damage, particularly at low impact energies where plastic deformation beneath the insert and sub-surface fractures predominates over chip mass removal. Various design parameters, including piston-to-bit mass ratio, piston length and impact velocity, were varied to evaluate their impact on the piston COR in pristine rock samples. Tests were conducted on granite, sandstone and limestone, all common rocks in down-the-hole hammer drilling. Despite variations in the impact energy level, the influence of mass or length ratios on the COR and the resultant destroyed rock volume was minimal. X-ray computed tomography revealed the significance of the crushed zone beneath the crater, affecting the rock ability to exert mechanical work on the bit during unloading. This characteristic led to the identification of a distinctive non-linear shape in the COR curves, with clearly delineated regions for each rock type, corresponding to different damage rates. These findings underscore the potential of the piston COR as a valuable tool for aiding in the identification of optimal drilling parameters and understanding rock formation characteristics during drilling.

Highlights

- Characteristic COR curves with clearly delineated regions as a function of the impact speed were established.
- Typical piston-to-bit length and mass ratios of DTH hammers have minimal influence on the COR and the rock damage.
- X-ray computed tomography revealed the significance of the crushed zone and side cracks in defining the non-linear shape of the COR curves.

Keywords Rock indentation · Dynamic load · Percussive drilling · X-ray computed tomography · Coefficient of restitution

1 Introduction

Percussive drilling is the most widely used method for drilling hard rocks, such as those found in mining deposits, quarries, geothermal and, to a lesser extent, civil engineering projects. The operational mechanism of these tools is based on a piston that repeatedly impacts a bit with a multitude of tungsten carbide inserts in contact with the rock (Chiang and Elías 2008). When the stress wave generated by the

✉ Jorge Aising
jorge.aising@minesparis.psl.eu

1 Mines Paris, Centre for Geosciences and Geoengineering, PSL University, Fontainebleau, France

2 Drillco Tools S.A., Santiago, Chile

3 Université de Pau et des Pays de L'Adour, E2S UPPA, CNRS, DMEX, Pau, France

4 Université de Pau et des Pays de L'Adour, E2S UPPA, CNRS, LFCR, Pau, France

Published online: 25 December 2024

impact reaches the inserts, they indent the rock at extremely high rates of deformation (Zhang 2004; Saadati et al. 2013; Aldannawy et al. 2022), leading to rock fragmentation if the piston impact velocity or the bit penetration achieved exceeds a certain threshold (Wijk 1989; Kwon et al. 2013; Jiang et al. 2020). Enhancing the efficiency of these tools has become essential nowadays to reduce energy consumption and carbon emissions in the industry (Gilbert et al. 2010). Therefore, understanding how to increase drilling efficiency, either by increasing the average drilling speed to generate more useful damage in each impact or by reducing air consumption, would result in a decrease in total energy expenditure by completing the drilling process in less time or consuming less fuel, respectively (Karpov and Timonin 2018). Clearly, both options depend on achieving increased destroyed volume with each impact at the same impact energy level. In this regard, various theoretical and numerical studies have focused on maximizing the transfer of energy in the impact between the piston and the bit, revealing how the length and mass ratios between the piston and bit affect the transfer of mechanical energy (Lundberg 1973; Changming 1991; Li et al. 2000; Lundberg and Collet 2010, 2015; Song et al. 2018; Yang et al. 2019). Unfortunately, few experimental works have been reported in literature on this topic. The work of Karlsson et al. (1989) systematically addresses the influence of piston-to-bit length ratios: by impacting a wedge bit indenter with a low impact velocity (close to 2 m/s), an optimal efficiency was obtained when the piston length equals the length of the bit. The efficiency is usually defined in these studies as the ratio between the net work done on the rock and the delivered energy or, through mathematical manipulations (Li et al. 2000), to the piston coefficient of restitution (COR). It is worth mentioning that, by their simple nature, these models cannot predict the volume or mass destroyed by the impact. To account for damaged volume, more sophisticated models using numerical techniques such as finite element method (FEM) or discrete element method (DEM) are required. These models can realistically simulate the piston–bit–rock interaction by modeling the rock fractured volume, giving insights into the drilling mechanism and helping in the design of experimental tests. Among these, Chiang and Elías (2008), using an FEM code, studied the effect of different DTH piston shapes, finding that the energy absorbed by the rock also depends on the piston geometry.

A simple way to assess the goodness or discrepancy of models such as those described, either theoretical or numerical, with real data is through efficiency indicators. The idea behind this is to reduce the output to a single value that can be easily compared or correlated with experimental and field trials. Among the efficiency indicators used for this purpose, the specific energy (SE) and the coefficient of restitution (COR) stand out. The concept of specific energy, initially introduced by Teale (1965), is defined as the energy required to remove a unit volume of rock material. Subsequently, various authors have used this concept to characterize their results; Li et al. (2020), through orthogonal experiments varying power, weight on bit (WOB), RPM, and bit type in a top hammer drill (THD) apparatus, found that hammer power is the most influential factor affecting the specific energy (SE) and the rate of penetration (ROP). Izquierdo and Chiang (2004) developed a specific system and method for DTH hammer rigs to monitor the SE while drilling. They observed significant variations of the SE along a borehole, suggesting its potential use to map or characterize the rocks as well as in identifying boundaries between different rock formations. Furthermore, they identified a quasi-linear correlation between SE and the operating frequency of the hammer. Despite its widespread acceptance, the concept of SE has some limitations: Ma et al. (2023) were unable to define a value for indentations smaller than 0.5 mm due to almost no mass removal when quantifying the damage caused by different indenters. In such cases, SE becomes undefined as it tends to infinity. On the other hand, the COR, which should be defined between 0 and 1 to satisfy the energy principle (Gilardi and Sharf 2002), also has some deficiencies. For instance, Hartman (1963) conducted experiments on intact rock to calculate the coefficient of restitution (COR) of a chisel bit that directly impacted the fresh surface of Bedford sandstone. However, he failed to find a clear trend providing useful information for characterizing the phenomenon. Therefore, he discarded the information as it did not align with the expectation that COR should monotonically increase with increasing impact energy. In a recent study, Lundberg et al. (2021) investigated the variation of the COR when impacting bars with short-duration forces in relation to the transit time in the bar, similar to those in THD. He found significant COR variation in such cases, sometimes exceeding unity. Consequently, selecting between these indicators is not straightforward.

This survey reveals a lack of experimental data available in the specific literature on DTH hammers, with most of the work being either numerical or theoretical. Moreover, when experimental research has been conducted, the configuration of piston–bit used is akin to a THD (Liu et al. 2017; Saksala et al. 2014). It is crucial to have reliable experimental data under various specific loading conditions for these tools, where the mass and the length ratios of the impactor to the bit typically fall within a range of 0.75–1.25. Parameters such as mass removed, crater diameter and depth are relevant for the mechanical design of the tools, while bit penetration, the length of radial cracks, among others, are relevant for calibrating specific simulation tools that allow exploration of designs under loading conditions not feasible to replicate in laboratory experiments (Kou et al. 2004). Additionally, it is convenient to explore efficiency indicators that easily

discriminate whether a drilling tool is operating at an optimal point. This study addresses these disparities by evaluating different piston-to-bit length ratios over a broad range of energies and impact velocities, including those characteristic of DTH-type tools. In Sect. 4.1, the influence of different piston-to-bit mass ratios on the piston COR were examined in each one of the three rock tested, and the limitations of the study were clearly outlined. A characteristic COR curve for each rock was established. In Sects. 4.2 and 4.3, by using X-ray computed tomography (XCT), the sub-surface fractures of the granite were correlated with changes in the COR curve, as well with the fragment size distribution. Then, in Sects. 4.4 and 4.5, by systematically increasing the impact energy, the effect on the rock damage and crater morphology was determined when using different piston-to-bit mass ratios. These results were correlated with the abrupt changes in the COR characteristics curve, and the possibility of using these results to identify optimal drilling operational points was discussed.

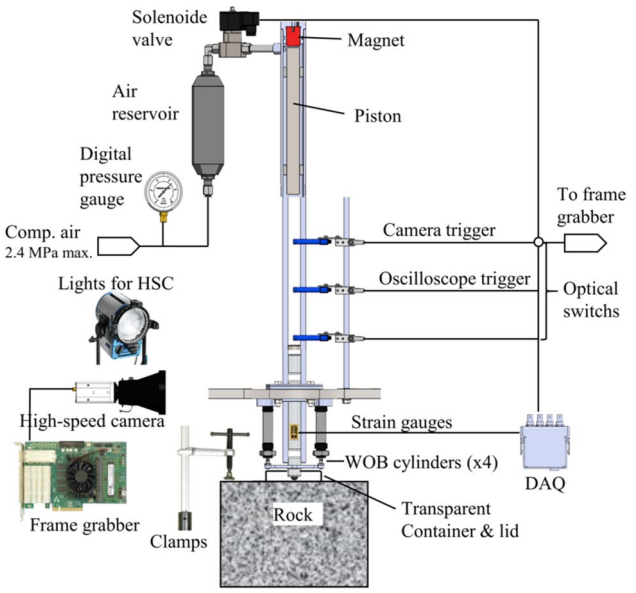

Fig. 1 Schematic of the experimental setup (redrawn from Aising et al. 2024a, b)

2 Experiment Description

2.1 Experimental Setup

An experimental gas-gun setup was developed, manufactured and assembled in the drilling laboratories of Mines Paris in Pau, France. This setup enables the precise firing of a piston onto a stationary bit placed atop a rock surface, achieving speeds ranging from 5 to 14 m/s. These velocities adequately cover the impact spectrum of percussive drilling tools. Moreover, for investigations requiring characterization of rock at lower impact energy levels, piston speeds below 5 m/s can be achieved by allowing the piston to free-fall from a height of 1.5 m. The firing pressure is controlled with software developed in LabVIEW, which also records WOB, impact velocity and rebound velocity. To accurately calculate impact and rebound velocities, a pair of photoelectric sensors positioned at a fixed distance from the impact position is employed. The light sensors utilized have a switching frequency of 4000 Hz, which, at an impact velocity of 10 m/s, yields a precision of ± 0.21 m/s (or ± 3.5 J at 75 J for a given piston mass of 1.173 kg) that is considered negligible for the purposes of this study. Figure 1 depicts the schematic of the experimental setup (redrawn from Aising et al. 2024a, b).

The time at which the impact occurs can be precisely determined by setting an ascending trigger on the stress signal obtained from a pair of strain gauges affixed to the center of the bit body. The stress signal and the signal coming from the photoelectric sensors were sampled at 20 MS/s, 14-bit resolution. Furthermore, the software handles communication with a high-speed camera, recording the entire interaction process between the tungsten insert and the rock at a high speed of 12,000 fps. Figure 2a depicts the progression of indentation in granite when the bit is impacted at a velocity of 11 m/s, allowing for the clear observation of the displacement of the bit and the chipping process. At the video acquisition rate, the maximum image size is 600×200 pixels, which, based on the actual field of view, corresponds to a raw resolution of 0.14 mm/px. Subsequent analysis harnesses this footage to reconstruct the indentation curve of the bit by tracking the movement of the insert. Figure 2b shows a zoomed-in section to the location of five tracking markers. Each marker represents the center point of a tracking windows with a size of 20×20 pixels. The cyan square around the tracking position in the upper left corner of Fig. 2b represents one of the sections undergoing tracking. While there is no standardized method for assessing the accuracy of a tracking method, we employed the approach described by Lückemann et al. (Lückemann et al. 2020), which involves quantifying the deviations in the distance between the points of a rigid body. As the distances must remain constant over time, the standard deviation can be used as an estimator of the accuracy of the method. Figure 2c shows the five trajectories used for this purpose, as well as three of the ten possible distance combinations utilized to calculate the standard deviations (d_{1-2}, d_{2-4} and d_{4-5}). When considering all ten combinations of vertical distances between the five markers, the average standard deviation achieved was 0.047 mm. Thus, the error in determining the position of the bit is ± 0.094 mm with a 95% confidence interval.

The visual record enables the observation of crucial events such as the occurrence of different types of cracks

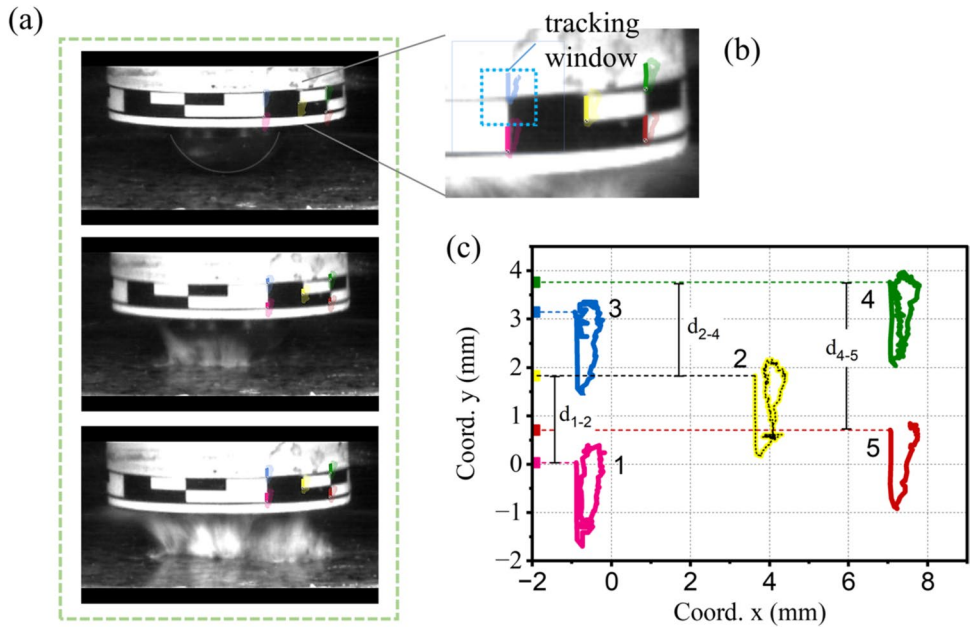

Fig. 2 **a** Frame-by-frame images of an impact in Kuru granite recorded at 12,000 fps, **b** zoomed-in view of the five tracked markers and **c** trajectories used to estimate the accuracy of the tracking method by computing the standard deviation of the vertical distance between each pair of tracked points

or the generation of large fragments. These observations are often indicative of the propagation of side cracks from beneath the crushed zone to the free surface of the rock. To prevent the loss of fragments and powder while simultaneously enabling recording, a transparent plastic container was attached to the bit. A tight fit between the lid of the container and the bit body was assured with an o'ring.

2.2 Rocks Tested

Three rocks in pristine condition were subjected to testing in this study: Kuru Grey granite (or simply Kuru granite) extracted from quarries in Finland, renowned for its high tensile and compressive strength; Rhune sandstone, extracted from quarries in southwestern France; and Saint Anne limestone, extracted from quarries in the Pyrenees region, southern France. Figure 3 shows macroscopic photos of the three rocks (Fig. 3a–c) as well their structure under cross-polarized light (Fig. 3d, e). Kuru granite

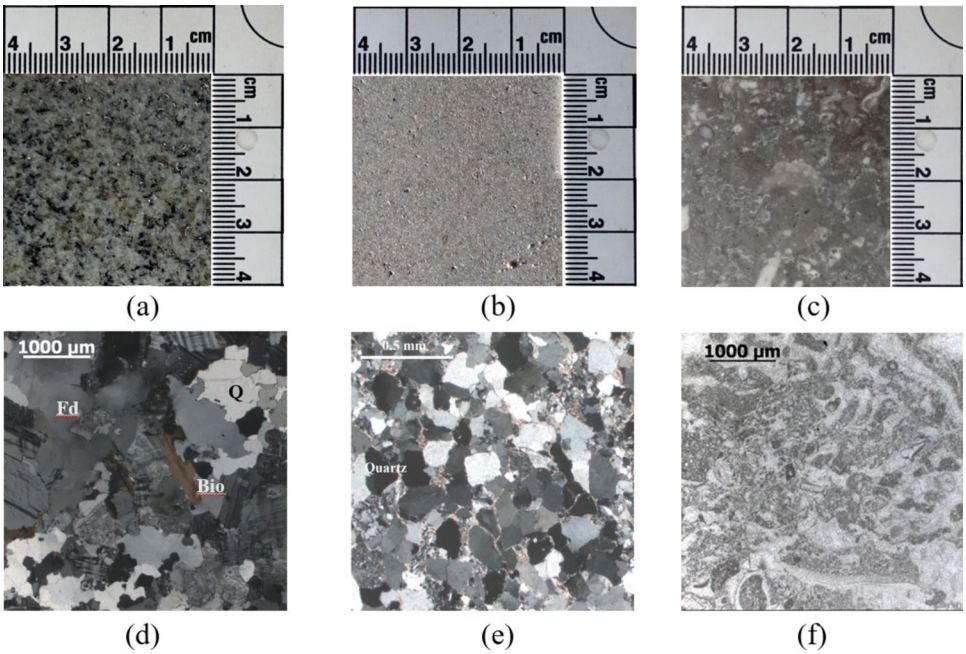

Fig. 3 Macroscopic view of **a** Kuru Grey granite, **b** Rhune sandstone and **c** Saint Anne limestone. Rock's structures under cross-polarized light for **d** Kuru Grey granite, **e** Rhune sandstone and **f** Saint Anne limestone. Pictures **d** and **f** redrawn from ORCHYD project work package 2 (Cazenave et al. 2021)

(Fig. 3a) exhibits isotropic behavior with heterogeneity at the scale of the insert radius, with grain size ranging from 0.3 to 1.5 mm, porosity of 0.33% and an average unconfined compressive strength (UCS) of 192 MPa and a indirect Brazilian tensile strength (BTS) of 11.4 MPa. Comprising about 60% feldspars, 35% quartz and 5% biotite (white, gray, and black, respectively, in Fig. 3a), its interlocking grains structure, which can be seen in Fig. 3d, confers high tensile strength (Dumoulin et al. 2024). Rhune sandstone is a homogenous fine-grained rock (Fig. 3b), grayish to greenish, with grains of detrital origin and 5.3% porosity. Its structure is predominantly composed of grains of quartz (94%) smaller than 0.2 mm (see Fig. 3e), with minor components of mica and muscovite (4%). Rhune sandstones exhibit a UCS of 137 MPa and a BTS of 5.48 MPa. Saint Anne limestone is a brecciated homogeneous rock, light gray to bluish gray, with bioclastic inclusions—such as shells and corals, white in Fig. 3c—and dispersed stylolites. The bioclastic inclusions may reach a size of 0.4 mm, while the calcareous matrix (micrite), which appears gray in Fig. 3c, is smaller than 0.01 mm (see Fig. 3f). It shows a UCS of 124 MPa and a BTS of 5.13 MPa. The density of the three rocks is similar, i.e., 2638 kg/m^3 for Kuru granite, 2535 kg/m^3 for Rhune sandstone, and 2732 kg/m^3 for Saint Anne limestone. Table 1 summarizes the mechanical properties of the three rocks obtained following the ISRM suggested method (Ulusay 2015). Average mechanical properties are illustrated in Fig. 4a where the number in parentheses denotes grain size. The dispersion of the BTS and the UCS are presented in Fig. 4b. The higher BTS variability observed in Kuru granite compared to the other rocks is directly correlated to its heterogeneity, particularly due to its larger grain size and local mineral composition (Zhang et al. 2023). For a comprehensive set of dynamic properties of Kuru granite, with or without confinement, the reader is referred to Dumoulin et al. (2024).

The samples were cut using a saw from hexagonal blocks of size 25 cm edge to edge. The height of each sample varied between 13 and 16 cm. The upper and lower faces were milled to ensure parallelism between them and perpendicularity to the vertical axis of the impact setup. Furthermore, to eliminate any potential interference with crack propagation or stress concentrations caused by traces left by the milling tool, the impact face was polished with stone discs ranging from 50 to 6000 grit, resulting in a

Table 1 Main rock mechanical properties for the three rocks

Rock	UCS (MPa)	BTS (MPa)	Grain size (mm)	ρ (kg/m^3)	E (GPa)	ν_p (m/s)	ϕ (%)	ν (m/m)
Kuru Grey	192	11.4	0.3–1.5	2638	56.94	4646	0.33	0.24
Rhune	137	5.48	< 0.2	2570	36.77	4452	5.3	0.20
Saint Anne	124	5.13	< 0.4	2732	70.68	5090	0.7	0.31

UCS unconfined compressive strength, *BTS* the unconfined tensile strength (Brazilian), ρ the density, E the Young's modulus, ν_p the P-wave velocity, ϕ the porosity and ν the Poisson's ratio

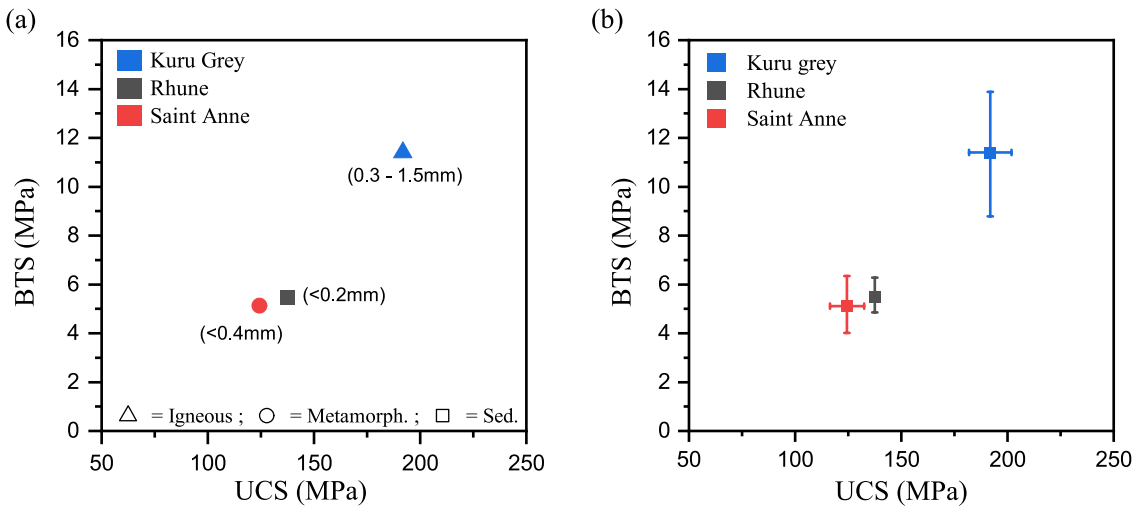

Fig. 4 **a** Brazilian indirect tensile strength versus compressive strength of the tested rocks. The number in parentheses denotes grain size, **b** compressive and tensile strength dispersion

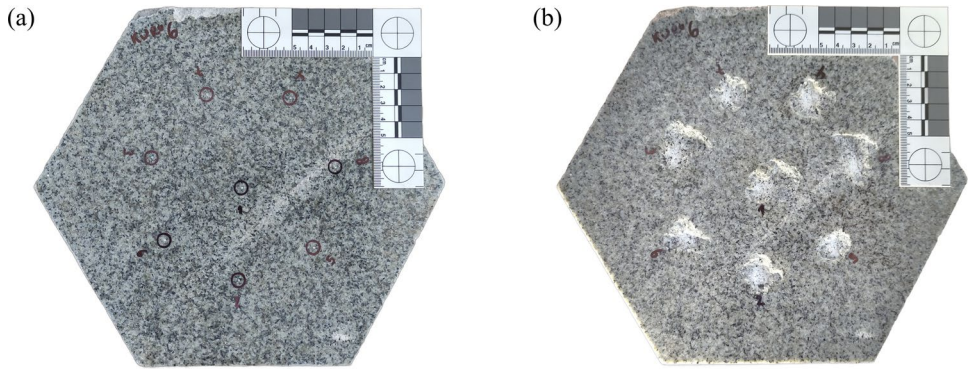

Fig. 5 **a** Front view of a Kuru Grey granite sample with the centers of the impact marked beforehand to aid in the positioning of the sample, **b** cleaned rock sample after impacts

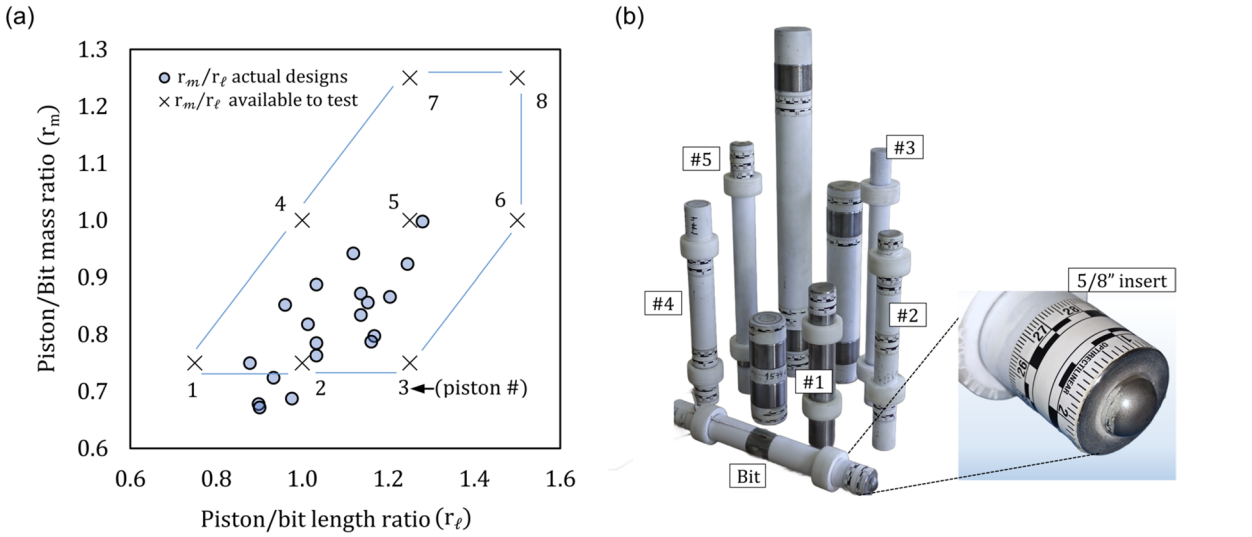

Fig. 6 **a** Piston-to-bit mass ratio versus piston-to-bit length ratio for DTH hammers in the 4-inch to 9-inch range. The blue circles represent actual hammer ratios, while the black crosses denote available piston mass and length ratios for use in the tests. **b** A picture of the bit and some of the available pistons for testing. The number denotes the piston/bit configuration

mirror-like finish. The impact locations were marked beforehand on the rock surface, as illustrated in Fig. 5a. To mitigate any size effects on the results, the impact centers were positioned at least 5 cm away from the free surface and from other impact locations (see Fig. 5b).

2.3 Piston-to-Bit Mass and Length Ratios

To investigate the effect of mass and length ratios between the piston and the bit, we defined a set of pistons with varying length and mass. These pistons were chosen to reflect, at the level of a single insert, the actual mass and length ratios found in commercial DTH hammers in ranges varying between 4 and 9 inch. In the same way, a 5/8″ carbide insert with hemispherical shape and an effective radius of 17 mm was fit-pressed at the end of the bit. This carbide insert configuration is commonly used in commercial drill bits in the specified bit range, as it offers an optimal balance between performance and tool life. The circles in

Table 2 Piston-to-bit length and mass ratios of several commercial DTH hammers ranging from 4 to 9 inch

Hammer size (inch)	r_ℓ (m/m)	r_m (kg/kg)	Hammer size (inch)	r_ℓ (m/m)	r_m (kg/kg)
4	1.17	0.80	6	1.15	0.86
	1.12	0.94		1.01	0.82
	1.03	0.89		1.24	0.92
	1.03	0.76	7	0.98	0.69
	0.96	0.85	8	0.90	0.67
	1.16	0.79		1.03	0.78
5	1.28	1.00		0.88	0.75
	1.20	0.87	9	0.93	0.72
	1.14	0.87			
	1.14	0.83			

Fig. 6a shows the length and mass ratios of commercial hammers (exact ratios can be seen in Table 2). A discernible trend emerges from these data, which can be attributed to the inherent design constraints of a hammer: once the hammer size is defined (typically of standard dimensions), increasing the mass often necessitates lengthening the piston due to the limited space available to enlarge the piston diameter. Black crosses in Fig. 6a represent the length and mass ratios of the set of pistons and bits available for testing, whose exact values, as well as the nominal length and mass, can be seen in Table 3. Despite the number of pistons available for testing, in this study, our attention focused on piston #2 ($r_\ell = 0.98$, $r_m = 0.76$), piston #4 ($r_\ell = 0.98$, $r_m = 1.0$) and piston #5 ($r_\ell = 1.23$, $r_m = 1.0$). Piston #2 and #5 were chosen as they represent the midpoint of the observed trend in commercial designs, and piston #4, with mass and length ratios equal to 1, because it is often regarded as an optimal combination (Lundberg 1985; Karlsson et al. 1989). Figure 6b illustrates some of the available pistons, as well as the bit with a 5/8″ spherical carbide insert used in all the tests. The number adjacent to the pistons indicates their respective configurations as depicted in Fig. 6a and in Table 3.

Table 3 Length, mass and piston-to-bit length and mass ratios (r_ℓ and r_m) of the pistons available for testing

Piston id	Length (mm)	Mass (kg)	r_ℓ (m/m)	r_m (kg/kg)
1	195	1.152	0.74	0.75
2	260	1.173	0.98	0.76
3	325	1.170	1.23	0.76
4	260	1.536	0.98	1.00
5	325	1.548	1.23	1.01
6	400	1.543	1.51	1.01
7	325	1.925	1.23	1.25
8	400	1.918	1.51	1.25

3 Measurement Techniques

3.1 Piston and Bit Displacement Curves

As shown in Fig. 7, the tracking of the bit and piston from high-speed videos allowed for the determination of displacement–time curves for each impact. In these curves, which offer comprehensive insight into each impact, the zero of the time axis has been aligned with the time of the impact for ease of reference. For the piston, it is possible to precisely determine the impact velocity v_{pi}, the instantaneous rebound velocity v'_{pr} and, in case of re-impact, the final rebound velocity v_{pr}. Re-impact occurs when the bit makes contact with the piston during the upward stroke, altering the piston coefficient of restitution (Li et al. 2000; Bu et al. 2009). The piston coefficient of restitution, COR, is defined as the ratio between the final piston rebound velocity and the piston impact velocity ($\mathrm{COR} = v_{pr}/v_{pi}$).

Regarding the bit, it is possible to determine the maximum bit indentation velocity v_{bi}, the maximum penetration u_m and the bit rebound velocity v_{br}. For the granite, it was found that v_{bi} was not constant even under the same piston impact velocity, possibly due to variations in the local stiffness of the rock at the scale of the insert's radius (Aldanawy et al. 2021). Furthermore, both u_m and v_{br} exhibit high dispersion, necessitating up to eight impacts per load condition to discern clear trends. The dispersion observed in v_{br} elucidates the differences obtained in the piston CORs. For example, the bit rebound velocities shown in Fig. 7a are

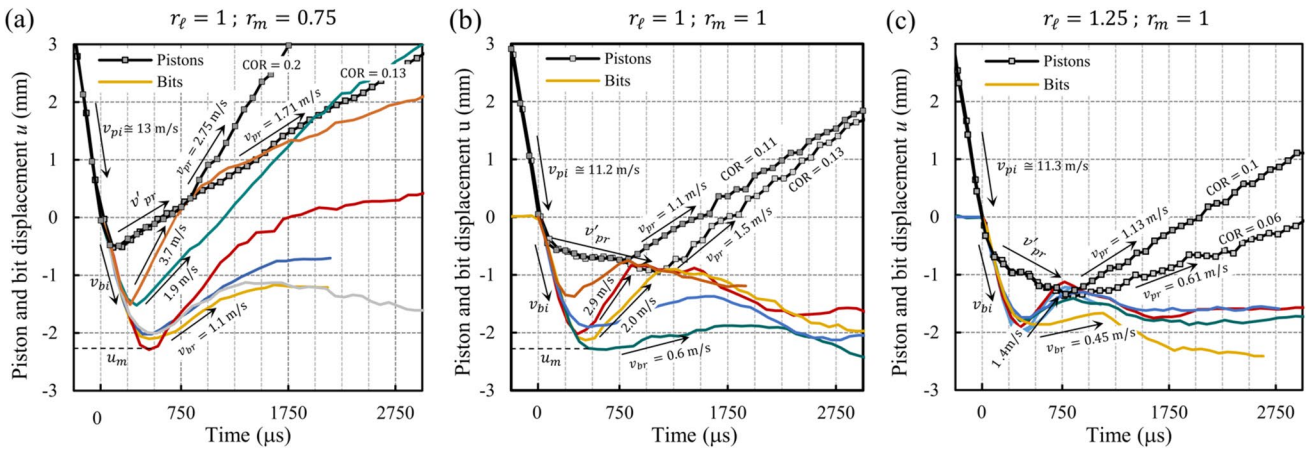

Fig. 7 Piston–bit interaction curves for different mass–length ratios. **a** $r_l = 1$, $r_m = 0.75$, **b** $r_l = 1$, $r_m = 1$, **c** $r_l = 1.25$, $r_m = 1$. Each curve corresponds to an impact on Kuru granite between 95 and 100 J. A high dispersion is observed in the bit rebound velocity zone due to varying levels of rock fragmentation

3.7 m/s, 1.9 m/s and 1.1 m/s. When the bit rebound velocity v_{br} was 3.7 m/s, it was sufficiently high to re-contact the piston. In this impact, which follows the principle of conservation of momentum because no external forces act on the colliding bodies, the piston rebound velocity increases from $v'_{pr} = 1.71$ m/s to $v_{pr} = 2.75$ m/s. Considering an impact velocity $v_{pi} = 13$ m/s, the piston COR is 0.2. Conversely, when the bit rebound velocity v_{br} was 1.9 m/s or 1.1 m/s, the bit cannot reach the piston, which moved away, resulting in no kinetic energy exchange or a very weak exchange. In these cases, a piston COR = 0.13 is observed.

In the case of pistons with ratios $r_\ell = 0.98$, $r_m = 1.0$ and $r_\ell = 1.23$, $r_m = 1.0$ (as depicted in Figs. 7b and 6c), a similar dispersion in v_{br} was observed (from 0.6 to 2.9 m/s in Fig. 7b, and from 0.45 to 1.4 m/s in Fig. 7c). Theoretically, the instantaneous piston rebound velocity v'_{pr} for both piston with ratios $r_m = 1.0$ should be exactly zero; however, both pistons tend to continue moving in the direction of the crater, approaching the bit rather than moving away. This tendency is more pronounced for the piston with $r_\ell = 1.25$ (Fig. 7c). This means that after the impact, any elastic recovery of the undamaged rock surrounding the crater—transferred to the bit in the form of kinetic energy—is always given back to the piston. In effect, the variation in the elastic recovery of the rock is the only plausible underlying mechanism driving the variability in the bit rebound velocity and, consequently, in the piston COR. Supporting the previous statement, as will be further discussed in Sect. 4.2, the dispersion observed in the bit rebound velocity is also correlated with a transition in the fragmentation of the granite and different levels of rock damage.

Similar displacement–time curves were obtained for Saint Anne limestone and Rhune sandstone, albeit with significantly lower dispersion in the results compared to those of the Kuru granite (see Sects. 4.1, 4.4 and 4.5). The consistency of the displacement–time curves and the low dispersion of the results in these two types of rocks underscores the reliability of the methodology employed. This also indicates that any dispersion in the results obtained in the granite tests arises from the interaction between the bit and the rock itself.

3.2 Crater Damage Morphology

The dust and fragments produced during each impact were meticulously collected with a soft bristle brush to avoid detaching fragments that were barely adhered to the rock surface. These fragments were weighed using a scale with a resolution of 0.001 g. Specifically for Kuru granite fragments, sieving was conducted to determine the size distribution based on the impact conditions. However, for limestone, sieving was considered unnecessary due to the poor distribution of the fragments, characterized by large rock pieces and minimum presence of powder. Similarly, for sandstone, although a mixture of fragments of varying sizes and rock powder was observed, sieve analysis was omitted because the impact velocities at which fragmentation starts were on the upper limit of the impact velocity of DTH hammers (11 m/s). Figure 8a–c illustrates the diverse fragmentation patterns in each rock. It can be observed that compared to granite (Fig. 8a) and sandstone (Fig. 8c), limestone exhibits minimal dust generation (Fig. 8b). This phenomenon has been attributed by Soussi et al. (2015) to the high quartz content present in the microstructure of granite and sandstone, along with their relative larger grain size, in contrast to the calcite content in the limestone.

After cleaning, various dimensions were measured to thoroughly characterize the crater. Figure 9a, b schematically shows the physical equivalent of each measurement in limestone/sandstone and in granite, respectively. These measurements include: (1) the length of the maximum radial crack L_{rc}; (2) the maximum crater length L_{max}; (3) the minimum crater length L_{min}; (4) the imprint diameter d_{imp}; (5) the maximum diameter of the crater d_{max}; (6) the

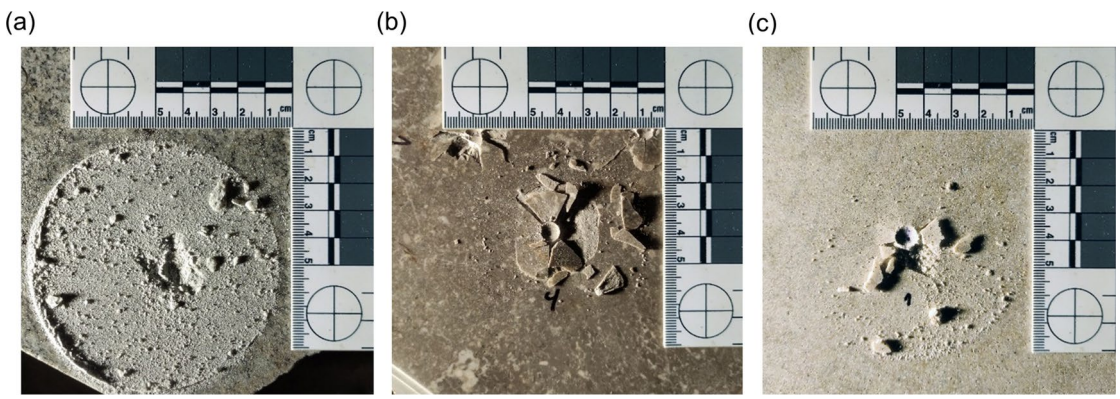

Fig. 8 Fragments lying on the rock surface prior to collection. **a** Kuru granite, **b** Saint Anne limestone and **c** Rhune sandstone

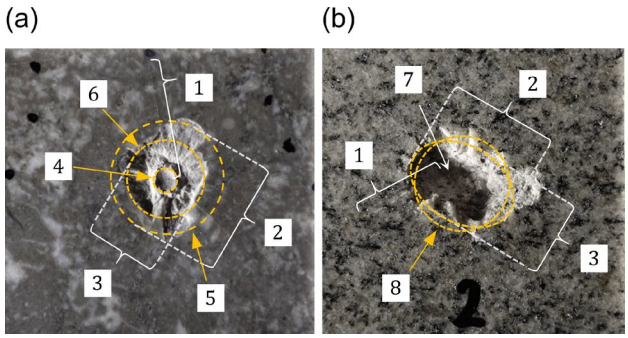

Fig. 9 Crater measurements in **a** limestone and sandstone **b** in granite. Figure nomenclature: **1** max. radial crack length; **2** max. crater length; **3** min. crater length; **4** imprint diameter; **5** max. crater diameter; **6** min. crater diameter; **7** crater depth; **8** equivalent crater diameter

minimum diameter of the crater $d_{\min}$; and (7) the crater depth d_c. All these measurements were recorded using a digital caliper immediately after cleaning the crater. Digital measurements from crater photos were also used to corroborate them. Due to the varying fragmentation behavior of each rock type, it was not always feasible to measure the same variables consistently across all samples. For instance, in sandstone or limestone, determining the depth of the crater was often challenging due to the persistence of a plastic imprint post-impact (labeled as 4 in Fig. 9a). Conversely, in granite, even at relatively low impact velocities, this zone was typically ejected, allowing the measurement of the crater depth (7).

The difference between crater diameters and crater lengths is that the former were measured centered to the impact's center, while the lengths could be off-center. Diameter measurements allow to determine when adjacent craters will connect under different impact energies, whereas lengths aid in defining a more representative crater area. For simple characterization, an equivalent diameter (8) was defined as $d_{eq} = \sqrt{L_{max} \times L_{min}}$, representing a circle diameter that equals the area of an ellipse of major and minor axis equal to L_{max} and L_{min}, respectively. This allows to effectively characterize the extent of crater damage with a single parameter.

After completing a series of impacts on a rock sample (typically eight impacts per sample), each sample was digitized at the CETIM Sud-Ouest laboratories in Pau, France, using a HandyScan Black portable laser scanner from Creaform, with an accuracy of 0.035 mm. Digitized the rock crater provides a precise representation of the surface to obtain accurate measurements such as crater depth, volume, morphology and roughness, among others (Mardoukhi et al. 2018; Mo and Li 2019; Aldannawy et al. 2021; Song et al. 2022). The output of the digitization process is a data file containing x, y and z coordinates representing each point of the surface. In most cases, the z-axis of the point cloud defining the rock surface was aligned with the impact direction; however, in some datasets, the surface of the sample was slightly misaligned. In such instances, to accurately measure the depth of each crater from a reference plane, a plane was fitted to the data, and the point cloud was rotated to ensure the alignment of the sample axis with the z-axis. The approximate center of each impact was identified automatically by detecting local minimums in the z values within a 50 mm-diameter moving window. It should be noted that the precise impact location does not necessarily coincide with the deepest point in the crater. For each crater, a surface was fitted using the Poisson surface reconstruction algorithm (Kazhdan et al. 2006) built-in in Matlab (see Fig. 10a–c). Following the method outlined by Al Danawwy et al. (2021), the crater volume and the surface area were calculated by numerically integrating the reconstructed surface.

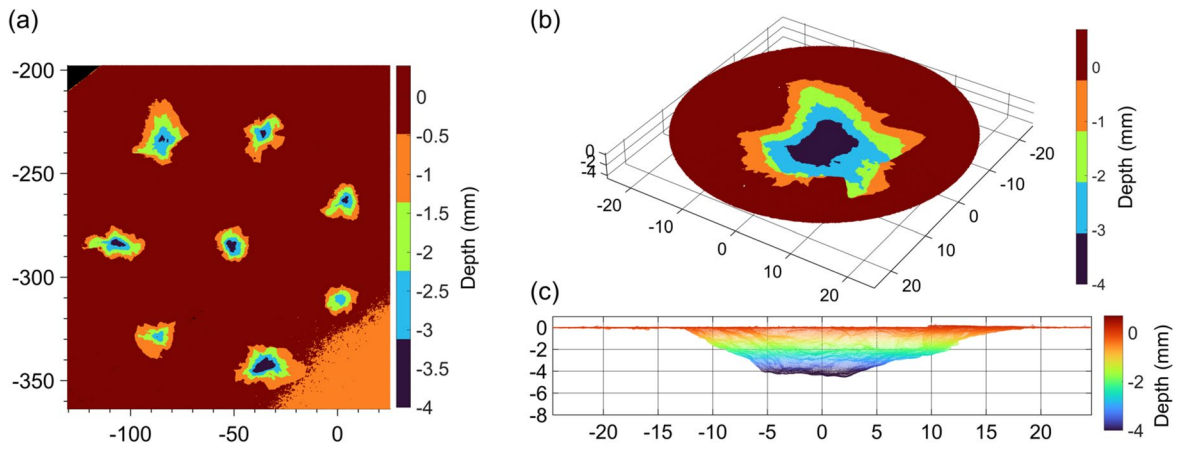

Fig. 10 **a** Digitization of a rock sample with eight impacts on its surface, **b** 3D view of a single crater, **c** lateral view of a single crater. For crater images, all axis units are in mm

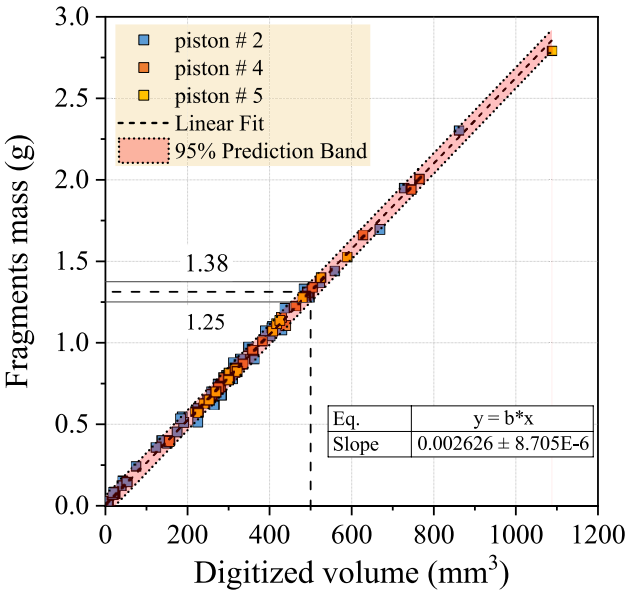

Fig. 11 Mass of the fragments against the volume of the digitized crater. The slope of the linear regression, representing the density of Kuru granite, deviates by 0.45% from the true value. The 95% confidence bands predict that for a digitized volume of 450 mm^3 the fragment mass spans from 1.25 to 1.38 g, representing a ± 4.75% variation from the expected value

The volume of the digitized craters was used to verify the fragment mass measurements. For example, Fig. 11 illustrates the linear regression between the mass of the weighed fragment and the crater volume obtained from the digitization of 89 craters (out of a total of 98 impacts). The data are presented according to the three pistons used, but the linear regression considers all data. A 95% prediction band was overlaid on the row data. The format of the fitted equation was $y = b \times x$ (i.e., constrained to intersect the origin). The slope of the fitted curve, which represents the density of the rock, was 2626 ± 0.87 kg/m^3. This value differs from the average value reported in Table 1 by only 12 kg/m^3 (0.45% difference). Regarding the error in measuring the fragment mass, as can be seen in Fig. 11, for a digitized volume of 450 mm^3, the mass of the fragments falls within a range of 1.25–1.38 g with 95% confidence, representing an error of ± 4.75% from the expected value. In conclusion for this part, the low error obtained indicates that the transparent container used prevented any significant loss of fragments, and than the procedure for collecting and weighing the fragments did not introduce significant errors in the results.

3.3 X-Ray Computed Tomography

To characterize the internal damage, some damaged granite samples, as depicted in Fig. 12, were scanned using X-ray computed tomography (XCT) at the DMEX Center for X-ray

Fig. 12 Core samples of Kuru granite scanned by XCT

Imaging, Pau University (UPPA), located in Pau, France. XCT is a non-destructive technique increasingly used in geosciences, because it allows obtaining three-dimensional representation of internal features such as mineral phases, porosity and internal fractures, without the need to cut the sample into sections (Cnudde and Boone 2013; Saur et al. 2020, 2021). This technique avoids potential alteration to cracks that may result from mechanical sectioning of the sample. In XCT, the sample is placed between an X-ray source and a detector. During the scanning process, a conical X-ray beam traverses the sample, capturing a series of 2D projection images from various sample orientations. The pixel values within these images reflect the intensity of the transmitted X-ray beam, and depend on the nature of the sample material, as expressed by the well-known Beer–Lambert law:

$$I = I_0 e^{-\mu h}, \tag{1}$$

where I_0 is the incident X-ray intensity, I is the intensity remaining after the X-rays pass through a sample of thickness h and μ is the linear attenuation coefficient which depends on the density and the atomic number of the sample material. Equation (1) is only valid when monochromatic light traverses a homogeneous medium. For non-homogeneous media, the term μh is replaced by the line integral along the beam path.

Preliminary tests to optimize scanning conditions were conducted using a Tescan UniTOM XL tomograph. This instrument is equipped with a polychromatic 300 W X-ray source adjustable between 30 and 180 kVp, along with a 16-bit flat panel capable of capturing images at 2856 × 2856 pixels. Regarding the resolution, three pixel sizes were tested (36, 26, and 15 µm), with 26 µm being selected due to its good trade-off between the field of view and resolution. The scans reported in this study utilized a 180 keV tube voltage, an effective target power of 26 W, a copper filter of 1.5 mm thickness and an exposure time of 3.5 s. For each scan, 2877 radiographs were acquired and used to reconstruct the 3D

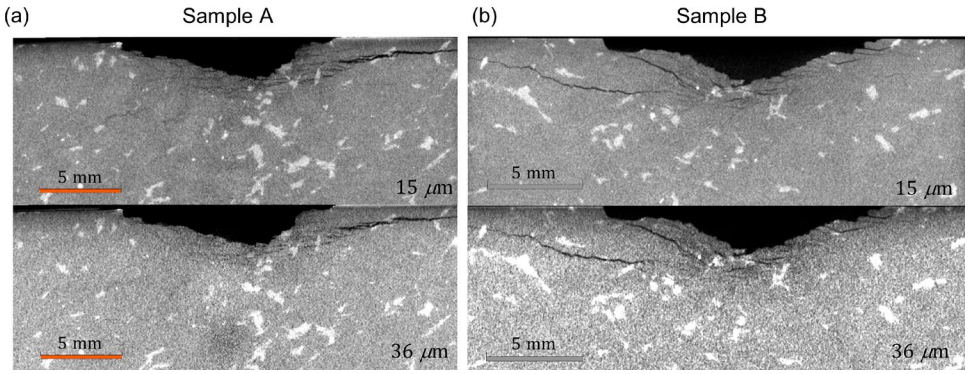

Fig. 13 **a**, **b** Comparison of XCT cross sections of granite core samples scanned at the highest and lower resolutions. Upper row: 15 µm. Lower row: 36 µm

datasets, which were subsequently visualized and analyzed using Dragonfly software 2022.2 (Comet Technologies Canada Inc., Montreal, Canada). Figure 13 shows the comparison between the resolutions of 36 and 15 µm in two different samples. Notably, any crack observable at a resolution of 15 µm (top row of Fig. 13) is also discernible at 36 µm (bottom row of Fig. 13), albeit with less sharpness. The sample diameters were 42 and 63 mm, depending on the crater extension.

4 Results and Analyses

This section presents the results obtained for each of the tested rock types. For Kuru granite, a total of 98 impacts were analyzed, while for Rhune sandstone and Saint Anne limestone, 19 and 39 impacts were analyzed, respectively. The significant difference in the number of tests between granite and the other two rocks lies in the high dispersion observed with the granite, requiring up to eight impacts per loading condition to observe discernible trends, whereas in the other two rocks, two or three impacts were sufficient. Depending on the observed level of fragmentation, the impact velocity was adjusted, either increased or decreased, to identify the velocity at which the crater began to form. In the case of the Rhune sandstone, fragment detachment was observed at an impact velocity greater than 11 m/s, a considerably higher value compared to the velocity required to initiate fragmentation in granite, nearing the limit of the piston strength. Consequently, this rock was characterized with a single mass ratio. For legibility, in the following sections, granite is used interchangeably with Kuru granite, sandstone with Rhune sandstone and limestone with Saint Anne limestone. Table 4 provides a summary of the testing conditions corresponding to the results shown in the figures from Sects. 4.1 to 4.5, grouped by rock type, rock sample and impact sequence number.

4.1 Characteristic Piston COR Curves

In this section, we focus on how to characterize the rocks by means of the piston coefficient of restitution (COR). We argue that utilizing the piston rebound velocity offers a more precise description of the damage compared to specific energy at low impact energies, where the plastic deformation and the crushed zone beneath the insert predominate over the mass removed (Ma et al. 2023). Figure 14a–c illustrates the measured piston COR values for each of the tested rocks at the three piston-to-bit ratios defined in Sect. 2.3. Several observations emerge, with the most notable being the existence of a characteristic COR curve with zones of high and low COR for each rock. In both limestone and granite (Fig. 14a, b), there are three clearly distinct zones, delimited by impact velocities v_1 and v_2. Velocity v_1 marks the point at which the crater starts to form, while velocity v_2 indicates the point where a discontinuity appears in the piston COR curve when a sufficiently high range of impact velocities is tested. The discontinuity represents an abrupt drop in the COR relative to the trend of the previous COR values. The first zone, from zero to v_1, exhibits the highest coefficient of restitution and negligible mass creation. The second zone, which extends from v_1 to v_2, is characterized by CORs evolving with a constant slope, either zero for limestone and sandstone, or slightly negative for granite. It will be demonstrated later in Sects. 4.4 and 4.5 that damage variables within this zone increase linearly as a function of the impact energy. The third zone, defined from v_2 and above, corresponds to a zone of low COR and high crater volume. For the limestone, v_2 starts approximately at 11 m/s. The average COR value for Saint Anne limestone before v_2 (i.e., high CORs values) considering the three piston-to-bit ratio tested is 0.44, while the average COR value for the high COR zone equals 0.10. For Kuru granite, v_2 is not clearly defined due to the dispersion within that zone, then it is best described as a transition zone. This transition zone starts at 9 m/s and ends approximately at 11.5 m/s. The mean CORs for the granite near the end of the transition and after the transition were 0.45 and 0.11, respectively. For the sandstone (Fig. 14c), only

Table 4 Summarized testing condition of the 158 impacts by rock type, rock sample and correlative impact number

Rock	Sample	Impact #	Impact speed (m/s)	Impact energy (J)	r_ℓ (m/m)	r_m (kg/kg)
Kuru Grey	K2	1 to 8	11.00 ± 0.08	70.9 ± 1.08	0.98	0.76
	K3	1 to 8	10.89 ± 0.07	69.7 ± 0.9	0.98	0.76
	K4	1 to 8	9.08 ± 0.06	48.4 ± 0.6	0.98	0.76
	K5	1 to 4	12.74 ± 0.08	95.2 ± 0.8	0.98	0.76
		4 to 8	13.27 ± 0.20	103.4 ± 3.5	0.98	0.76
	K6	1 to 4	13.39 ± 0.07	105.2 ± 0.8	0.98	0.76
		5 to 8	9.36 ± 0.06	51.3 ± 0.6	0.98	0.76
	K7	1 to 8	11.42 ± 0.09	76.6 ± 1.4	0.98	0.76
	K8	1 to 5	13.40 ± 0.13	105.3 ± 1.3	0.98	0.76
	K9	1 to 8	11.26 ± 0.12	98.1 ± 2.0	1.23	1.01
	K10	1 to 8	11.22 ± 0.02	96.8 ± 0.2	0.98	1.00
	K11	1 to 4	12.72 ± 0.02	124.2 ± 0.6	0.98	1.00
		5 to 8	9.71 ± 0.03	72.4 ± 0.2	0.98	1.00
	K12	1 to 4	13.62 ± 0.20	143.7 ± 3.8	1.23	1.01
		5 to 8	10.42 ± 0.03	84.0 ± 0.4	1.23	1.01
	K13	1 to 2	4.75 ± 0.00	13.26 ± 0.01	0.98	0.76
		3 to 4	5.68 ± 0.01	18.91 ± 0.04	0.98	0.76
		5 to 7	6.55 ± 0.02	25.19 ± 0.12	0.98	0.76
		8 to 10	7.32 ± 0.02	31.46 ± 0.18	0.98	0.76
		11 to 13	8.04 ± 0.03	37.93 ± 0.20	0.98	0.76
Saint Anne	S2	1 to 2	6.23 ± 0.00	22.8 ± 0.02	0.98	0.76
		3 to 4	4.63 ± 0.00	12.6 ± 0.01	0.98	0.76
		5 and 7	3.55 ± 0.04	7.4 ± 0.15	0.98	0.76
		6 and 8	2.48 ± 0.02	3.59 ± 0.07	0.98	0.76
	S3	1 to 2	9.41 ± 0.06	51.9 ± 0.64	0.98	0.76
		3 to 4	8.07 ± 0.00	38.2 ± 0.02	0.98	0.76
		5 to 6	7.35 ± 0.01	41.8 ± 0.1	1.23	1.01
		7 to 8	5.50 ± 0.00	23.37 ± 0.02	1.23	1.01
		9 to 10	3.70 ± 0.00	10.60 + 0.00	1.23	1.01
		11 to 12	2.37 ± 0.00	4.35 ± 0.02	1.23	1.01
	S4	1 to 2	8.89 ± 0.00	61.17 ± 0.04	1.23	1.01
		3 to 4	8.12 ± 0.03	51.06 ± 0.35	1.23	1.01
		5 to 6	7.15 ± 0.01	39.25 ± 0.07	0.98	1.00
		7 to 8	5.63 ± 0.04	24.35 ± 0.30	0.98	1.00
	S5	1 to 2	8.80 ± 0.05	59.44 ± 0.69	0.98	1.00
		3	10.00 ± 0.00	76.9 ± 0.00	0.98	1.00
		4 to 5	11.88 ± 0.04	82.75 ± 0.59	0.98	0.76
	S6	1	10.00 ± 0.00	76.9 ± 0.00	0.98	1.00
		2 to 3	10.39 ± 0.03	85.53 ± 0.53	1.23	1.01
		4	8.92 ± 0.00	61.1 ± 0.00	0.98	1.00
		5	10.66 ± 0.00	66.7 ± 0.00	0.98	0.76
	S7	1 to 2	12.25 ± 0.00	116.1 ± 0.00	1.23	1.01
Rhune	R2	1 and 4	13.09 ± 0.01	100.4 ± 0.23	0.98	0.76
		2 and 3	13.96 ± 0.05	114.3 ± 0.82	0.98	0.76
		5 to 6	12.08 ± 0.01	85.5 ± 0.07	0.98	0.76
		7 to 8	11.00 ± 0.01	70.96 ± 0.12	0.98	0.76
		9 to 10	9.74 ± 0.00	55.65 ± 0.01	0.98	0.76
		11 to 12	8.43 ± 0.00	41.64 ± 0.04	0.98	0.76

r_ℓ and r_m are the piston-to-bit length and mass ratios

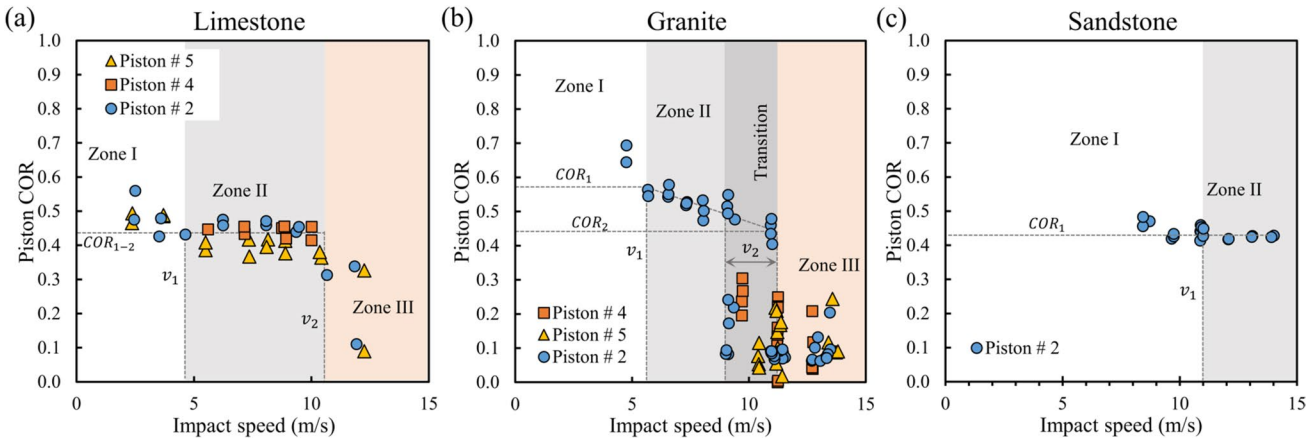

Fig. 14 Piston coefficient of restitution (COR) as a function of the piston impact speed for the set of rock tested: **a** limestone, **b** granite, **c** sandstone

Table 5 Impact velocities and COR defining zone II and zone III

Rock type	Zone II (high COR)				Zone III
	v_1 (m/s)	COR_1	v_2 (m/s)	COR_2	Low COR
Limestone	4.6	0.44 ± 0.05	10.4	0.44 ± 0.05	0.10 ± 0.02
Granite	5.4	0.56 ± 0.02	11.5	0.45 ± 0.03	0.11 ± 0.07
Sandstone	11.0	0.43 ± 0.02	Not observed		

zone I and a portion of zone II were observed, although it is expected that future tests at higher impact velocities will allow the determination of v_2. Then mean COR for Rhune sandstone in the observable region of zone II was equal to 0.43. Table 5 summarizes the range of values defining v_1 and v_2, as well as the corresponding COR values for each rock. These values and their corresponding sections are also depicted in Fig. 14a–c. Notably, none of the velocities defining these zones are influenced by the different piston-to-bit ratios tested.

Based on the similarities observed between zone I characteristics and the COR curves presented by Goldsmith (1960) for impacts involving spheres of differing materials at velocities up to approximately 6 m/s (thus indicative of zone I), it can be concluded that the COR value increases gradually from its value at v_1 to 1 as the impact velocity approaches zero, indicating that when a rock is impacted at $v \approx 0$, its elasticity remains intact because the internal damage is near zero, making the COR a reliable indicator of the damage progression within the rock, offering advantages over the specific energy as a metric.

To the best knowledge of the authors, no published literature exists on the rock COR non-linearity presented in this paper. The existence of these curves has at least two direct implications.

First, from a hammer design perspective, it would be possible to tailor a hammer to each rock being drilled, as it is evident that an optimum in impact energy exists around the discontinuity, although it is not possible from these single impact experiments to know which point exactly is. For example, as a first option, a hammer operating at the point immediately after the discontinuity in the COR curves at v_2 will create larger craters per impact, but with few cracks below the surface (see Sect. 4.2). In a second option, a hammer operating just before the discontinuity at v_2 will create a rich network of cracks beneath the crushed zone, which can be beneficial on a real-scale hammer with successive impacts and multiple carbide inserts. This, along with the expected higher percussion frequency of the hammer as a consequence of a higher COR (Izquierdo and Chiang 2004), could lead to a similar hammer optimum. To discriminate the optimum between the two options, a field test should then be conducted at real scales.

Second, even in DTH hammers with a low mass ratio, such as most commercial DTH hammers and the piston # 2 ($r_l = 1$, $r_m = 0.75$) tested here, it would be possible to identify different types of rock formations while drilling by measuring the COR in real time. To accomplish this, it is a necessary condition that there is re-contact between the bit and the piston, allowing information about the elastic recovery of the rock to be transferred to the piston, and that these results, obtained in laboratory conditions, persist in a real drilling environment.

While this study provides valuable insights into the elemental bit–rock interaction using a single insert and single impact configuration with pristine rocks, it does not fully capture the complexity of DTH drilling operations, where multiple inserts interact with rock already fractured by

previous impacts (Aising et al. 2024a, b; Liu et al. 2008). This simplified approach was chosen to isolate the specific variables related to percussive hammer design (piston mass, impact energy, insert radius) from the previous state of the rock and avoid misinterpreting their influence on the results. Although these findings can guide hammer designs or calibrate numerical tools, full-scale testing is necessary to validate their persistence in real operations.

4.2 XCT Granite Internal Damage Characterization

To analyze the evolution of the sub-surface damage and assess potential correlations with the COR curves discussed earlier in Sect. 4.1, eight core samples of Kuru granite impacted by piston # 2, aiming to represent the COR in each of the three zones, were selected for XCT characterization as described in Sect. 3.3. For identification purposes, each selected sample was labeled as *Km-n*, where *m* indicates the rock block, and *n* the *n*-th impact on it. Columns (a) and (b) in Fig. 15 show different XCT cross-sectional images passing through the axis of the impact. Each row corresponds to a distinct impact velocity, organized based on the zones identified in Sect. 4.1. To facilitate the interpretation of the figure, all images have the same scale. In Fig. 15, the left column (a) contains images representing the high segment of the COR curve, while the right column (b) displays images

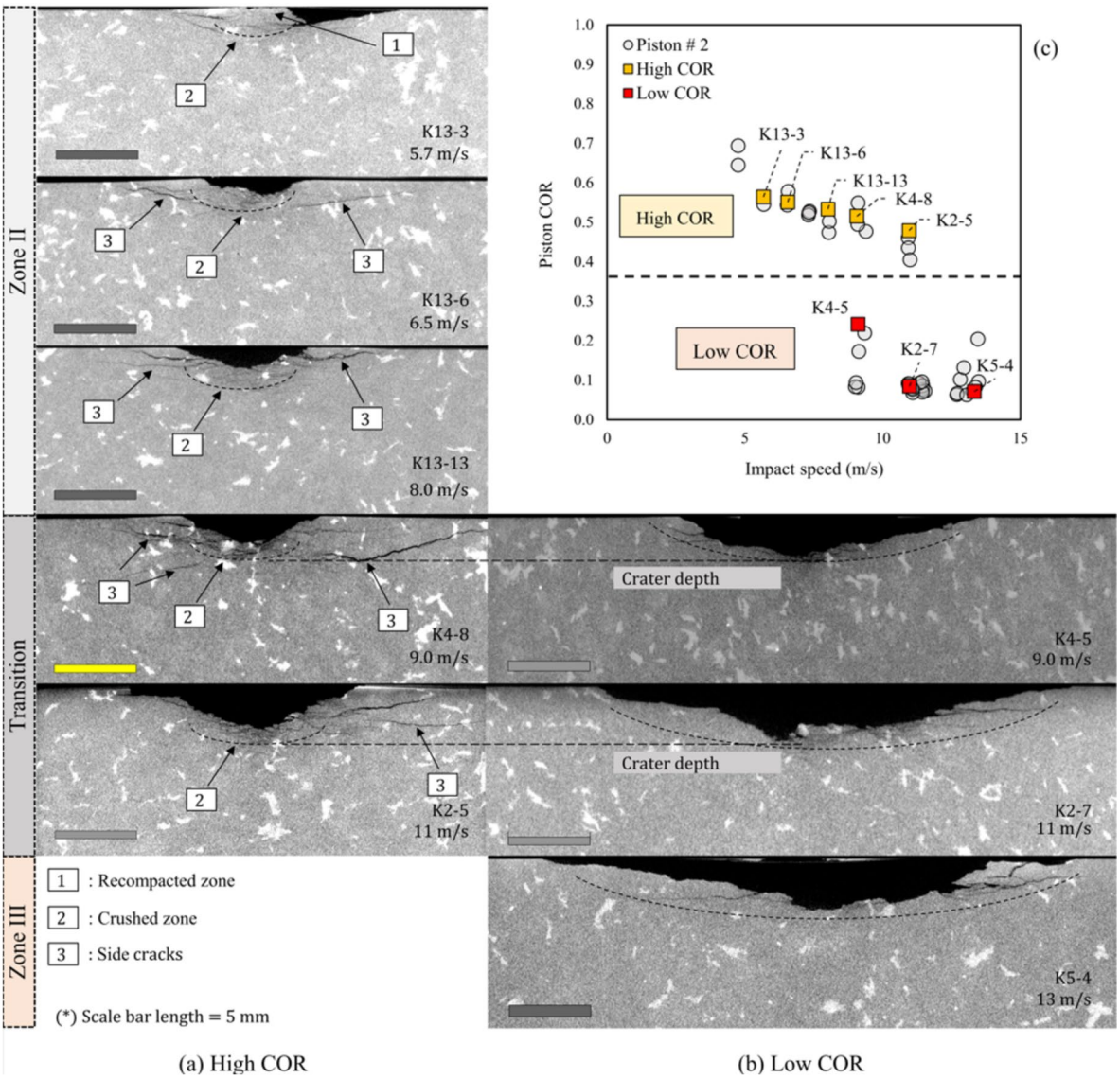

Fig. 15 XCT cross sections of Kuru granite samples loaded at different impact energies. Column **a**: samples with a high coefficient of restitution. Column **b**: samples with low coefficient of restitution. **c**: piston COR versus impact speed. Yellow squares indicate samples with high COR and red squares indicate samples with low COR. The high COR of samples K4-8 and K2-5, compared to samples K4-5 and K2-7, is attributed to the persistence of the crushed zone after the impact

corresponding to low COR. The graph showing the selected samples with high COR (yellow squares) and low COR (red squares) among all the samples is shown in Fig. 15c. For impact velocities of 9 and 11 m/s (denoted as the transition zone), the XCT cross sections are presented side by side to facilitate the comparison of crushed zones and crater depths. For this purpose, segmented straight lines have been drawn across the images (see cross sections of samples K4-8 and K4-5, and samples K2-5 and K2-7).

Figure 15 qualitatively illustrates that specimens with a high COR (Fig. 15a) exhibit internal damage characterized by a crushed zone extending deep beneath the crater, alongside multiple side cracks nucleating from different depths and propagating to a length greater than the corresponding crater radius. Conversely, samples exhibiting low COR values (as shown in Fig. 15b) demonstrate internal damage characterized by the absence of a crushed zone and minimal presence of residual side cracks. Furthermore, it is evident that given the same impact speed, samples with a low COR present more extracted mass in comparison to samples with a high COR.

To provide quantitative support for the visual observations outlined earlier, Table 6 summarizes several measurements extracted from the XCT images depicted in Fig. 15, while Fig. 16a–f presents graphical representations of these measurements. The key measurements summarized in Table 6 comprise the bit penetration (obtained from the displacement curves), the depth of the crushed zone, the depth of the crater, the length and depth of the side cracks and the maximum radius of the crater. From Fig. 16a it can be observed that the depth of the crushed zone exhibits a linear relationship with the impact velocity across most of the range of velocities, except for zone III where it does not show significant increase. Regarding the depth of the crater, it is observed that in the transition zone at v_2, the depth of the crater increases randomly but upper bounded by the crushed zone depth, as the crater expands to the volume left by the random ejection of the crushed zone (See the XTC cross section of Fig. 15a, b in the transition zone).

Similarly, Fig. 16b shows that to the left of the transition zone, the radius of the crater is consistently smaller than the length of the corresponding side crack. However, this relationship changes in the transition zone, where both variables become equal. This indicates that the side cracks, which were kept below the surface at lower impact velocities, have now emerged to the surface, producing fragments and consequently enlarging the radius of the crater and the extracted mass.

Figure 16c illustrates the relationship between drill bit peak force, crater depth and crushed zone depth. The depth of the crushed zone was found to be linear with respect to the drill bit force for forces in zone I, zone II and the transition zone. The crater depth exhibits a linear trend for forces below 114 kN; as for the transition zone, the crater depth values jump to follow the trend of the crushed zone depth. Both variables apparently have a cutoff for forces exceeding 139 kN, meaning further increases in force do not result in proportional gains.

In summary, the comparison of samples K4-8/K4-5 and K2-5/K2-7, each pair impacted at the same velocity, reveals that the cause for the low COR in samples K4-5 and K2-7 lies in the removal of material around the insert and the consequent release of energy. Hence, the discontinuity in the COR characteristic curves in Fig. 14 is primarily attributed to two changes in the fracture mode: (1) the pulverization and ejection of the crushed zone and (2) the formation of large fragments due to the coalescence of radial and side cracks on the rock surface. While the energy dissipation associated with the creation of new free surfaces as cracks expand to form large fragments elucidate the lower COR from an energetic standpoint, the loss of material around the insert, which prevents any elastic recovery that the rock can exert on the bit, explains the same phenomenon from a mechanical perspective. As postulated in Sect. 4.1, the absence of a fractured zone, the relatively low presence of

Table 6 XCT sub-surface characterization

	Impact speed (m/s)	Granite Sample	Bit penetration (mm)	Crushed zone depth (mm)	Crater depth (mm)	Max. side crack length (mm)	Side crack depth (mm)	Crater radius max. (mm)
Zone II	5.68	K13-3	0.48	1.4	–	6.2	1.1	–
	6.55	K13-6	0.61	1.6	1.0	8.5	1.4	5.3
	8.04	K13-13	0.62	2.4	1.1	8.9	1.3	7.6
Transition	9.08	K4-8	0.97	2.6	1.6	15.0	2.5	8.9
	11.0	K2-5	1.00	3.3	2.3	15.6	2.3	9.0
	9.08	K4-5	1.02	2.7	2.6	9.9	1.4	9.8
	11.0	K2-7	1.12	3.2	3.1	16.2	3.0	16.4
Zone III	13.3	K5-4	2.24	3.1	3.3	16.9	3.2	19.1

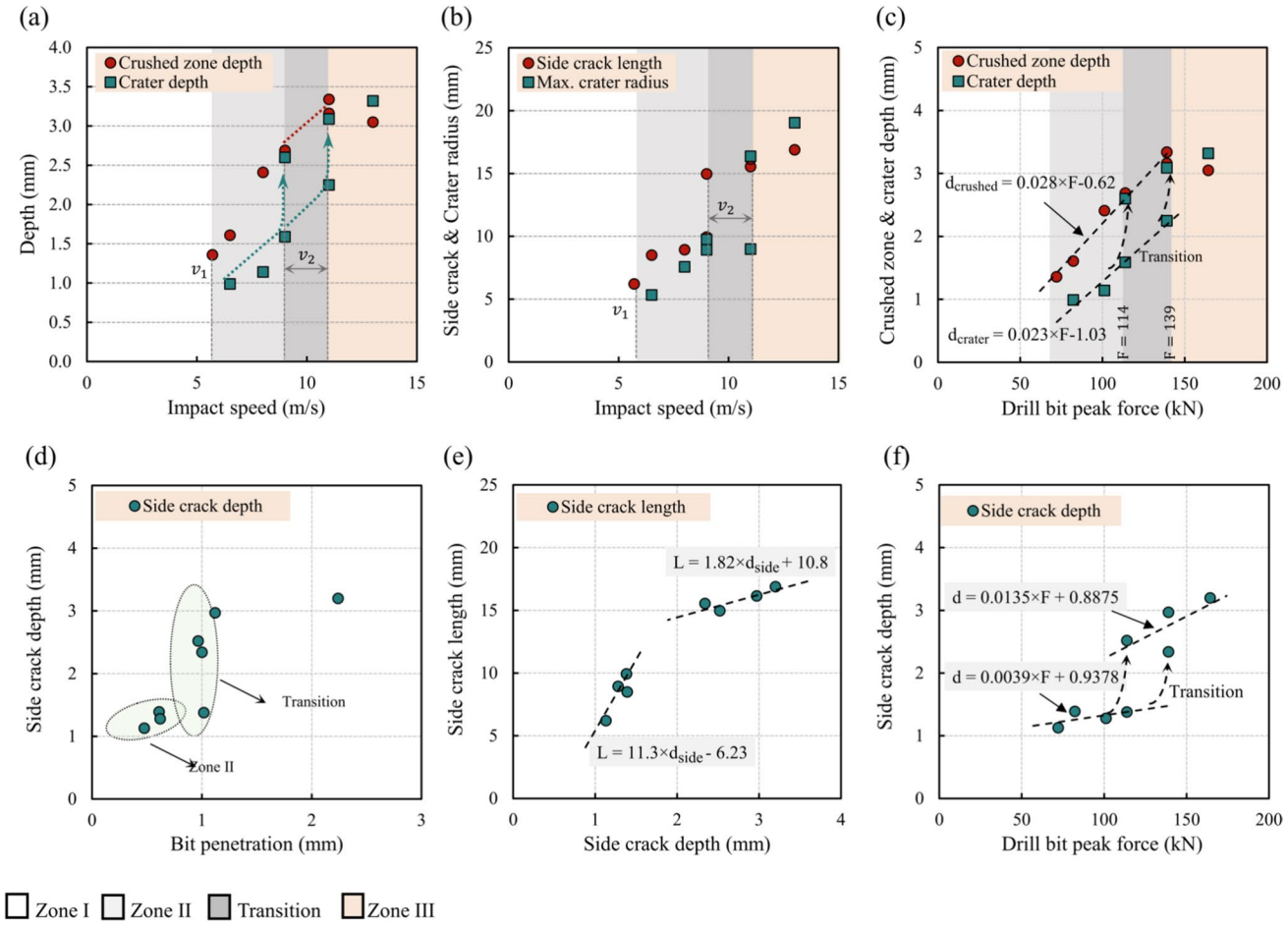

Fig. 16 **a** Crushed zone depth and crater depth as a function of impact speed, **b** length of the primary side crack and the maximum crater radius as a function of impact speed, **c** crushed zone depth and crater depth as a function of the drill bit peak force, **d** depth of the primary side crack versus bit penetration, **e** length versus depth of the primary side crack and **f** depth of the primary side crack versus drill bit peak force

side cracks and the higher crater volume indicate that this zone could represents one of the two optimal working areas for a roto-percussive tool, since subsequent impacts are likely to occur on a surface relatively free of defects, thus minimizing regrinding and enhancing crack propagation.

Other interesting relationships that contribute to the clarification of the mechanism promoting the generation of large fragments emerge from plotting the depth at which the main side cracks nucleate and their respective lengths as a function of bit penetration and drill bit force. For the first, it is observed from Fig. 16d, that within the transition zone, a discrete jump—nearly vertical—in the depth of the side cracks from approximately 1.4 mm to more than 2.5 mm occurs under a constant penetration of the bit (around 1 mm). From there, the depth of the side cracks does not seem to increase drastically, and remains around 3 mm. XTC images of Fig. 15 reveal that the shallow (less than 1.4 mm) and deep side cracks (more than 2.5 mm) were generated from different regions (and likely at different times) during the indentation. The most plausible explanation for this change has been postulated by Liu et al. (2008) through numerical simulations: The change in depth arises from the fact that depending on the impact speed, the side cracks may nucleate either from the skirt of the Hertzian cone (low impact speeds, shallow side cracks), or from the base of the crushed zone (high impact speed, deep side cracks).

Regarding the side crack length, Fig. 16e illustrates a direct relationship between the depth at which a side crack was generated and its length: the deeper the crack, the greater is its length. Additionally, considering the slopes of the trends (refer to the slopes of the linear regressions in Fig. 16e), it can be observed that the growth rate reduced more than six times (from 11.3 to 1.82 m/m) when side cracks originate at depths exceeding 2.4 mm. On the other hand, Fig. 16f shows that as the drill bit force is increased (by increasing the piston impact speed), the depth at which the side cracks are generated increases in a linear stepwise manner, with the transition zone defining the force range

at which the depth of the side crack becomes significantly deeper. Taken together, these three observations reveal that beyond the transition zone (i.e., impact velocity larger than v_2 or impact force larger than 139 kN), the enlargement of the crater diameter due to the increase of the side crack length, and hence the mass removed, becomes less effective.

4.3 Sieve Analysis

Fragments collected from six granite samples were sieved to aid in understanding the non-linearity of the COR curves and their correlation with the detachment of large fragments. Large fragment creation is often desirable in drilling as the energy associated with their creation is minimal (Lawn and Wilshaw 1975; Saksala 2011). The sieved samples correspond to those presented in the previous section, with impact velocities of 9, 11 and 13 m/s, making them representative of the transition zone and zone III. Eight sieves ranging from 0.08 to 9 mm according to ASTM E11 specifications were utilized. Fragments larger than 9 mm were not obtained, and hence the results are shown only up to 4.5 mm. Figure 17a–c illustrates the cumulative mass fraction curves for each velocity, while Fig. 18 presents a graphical comparison of the fragments retained in each mesh. For each curve, the coarseness index (CI) was calculated, serving as a descriptor of the average size of the fragment distribution. In all cases, a coarser fragment distribution is evident when a lower COR is achieved. Since higher CI values have been successfully correlated with high drilling efficiency (Altindağ 2003; Reyes et al. 2015), the notion that there is an optimal operating point for a rotary percussive tool exists—where the COR drops abruptly—is reinforced. However, when observing in Fig. 18 the gross amount of fragments retained in each mesh, it is observed that the increase in coarser fragments is accompanied by an unwanted increase in the fines retained on the smaller meshes. Based on the remaining side cracks in the high COR XCT samples shown in Fig. 15a, it is reasonably clear that the additional dust comes not only from the crushed zone, but also from dust trapped between the new surfaces created by the propagation of the side cracks. This dust is released when fragments detach, contributing to the observed increase in fines.

4.4 Bit Penetration and Crater Mass Results

As mentioned in the introduction, many studies on drilling optimization (Chiang and Elías 2008; Depouhon et al. 2015; Lundberg and Huo 2017) have focused on predicting crater mass and bit penetration. Consequently, experimental data are crucial for calibrating such as numerical tools (Kou et al. 2004), and evaluating the potential performance of percussive tools (Fourmeau et al. 2017; Jiang et al. 2020).

In this study, for each type of rock and piston length, the bit penetration was determined from displacement curves derived from high-speed recordings (see Sect. 3.1). The maximum bit penetration and the crater mass values from the 158 tests performed are shown in Fig. 19. Instead of plotting trend lines, individual results were plotted to avoid obscuring the dispersion of the results and, to a certain extent, explicitly illustrate the effect of different degrees of rock heterogeneity in the outcomes. Each column represents results obtained from limestone, granite and sandstone. Rows 1, 2 and 3 display the bit penetration as a function of impact velocity, bit penetration as a function of impact energy and the crater mass as a function of impact energy, respectively. The critical impact velocities—or the equivalent impact energy—defining the characteristic COR curve of each rock, were drawn on these graphs to help identify

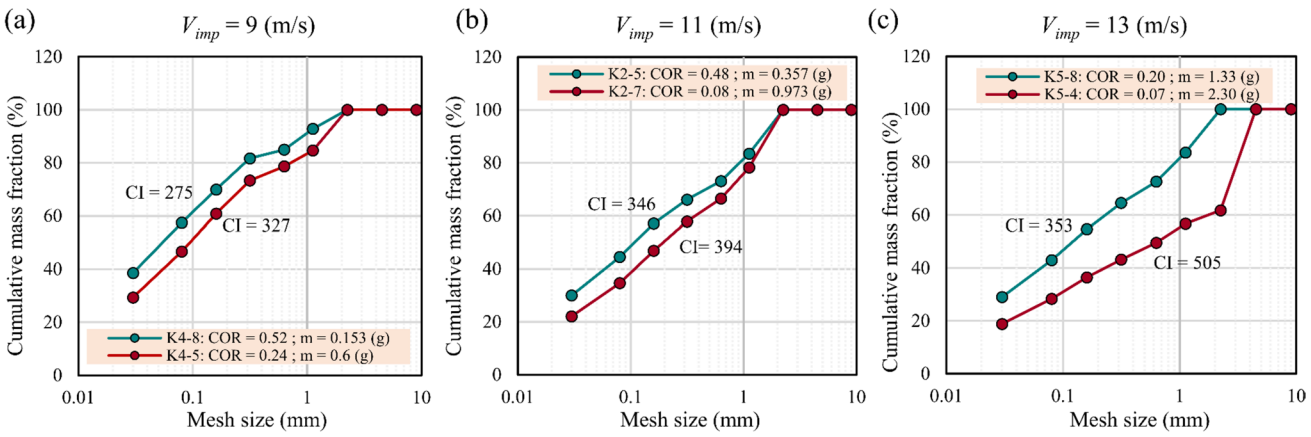

Fig. 17 Cumulative fragment mass distribution of samples impacted at the same impact speed, but with different piston COR. **a** Impact speed equal to 9 m/s, **b** impact speed equal to 11 m/s and **c** impact speed equal to 13 m/s

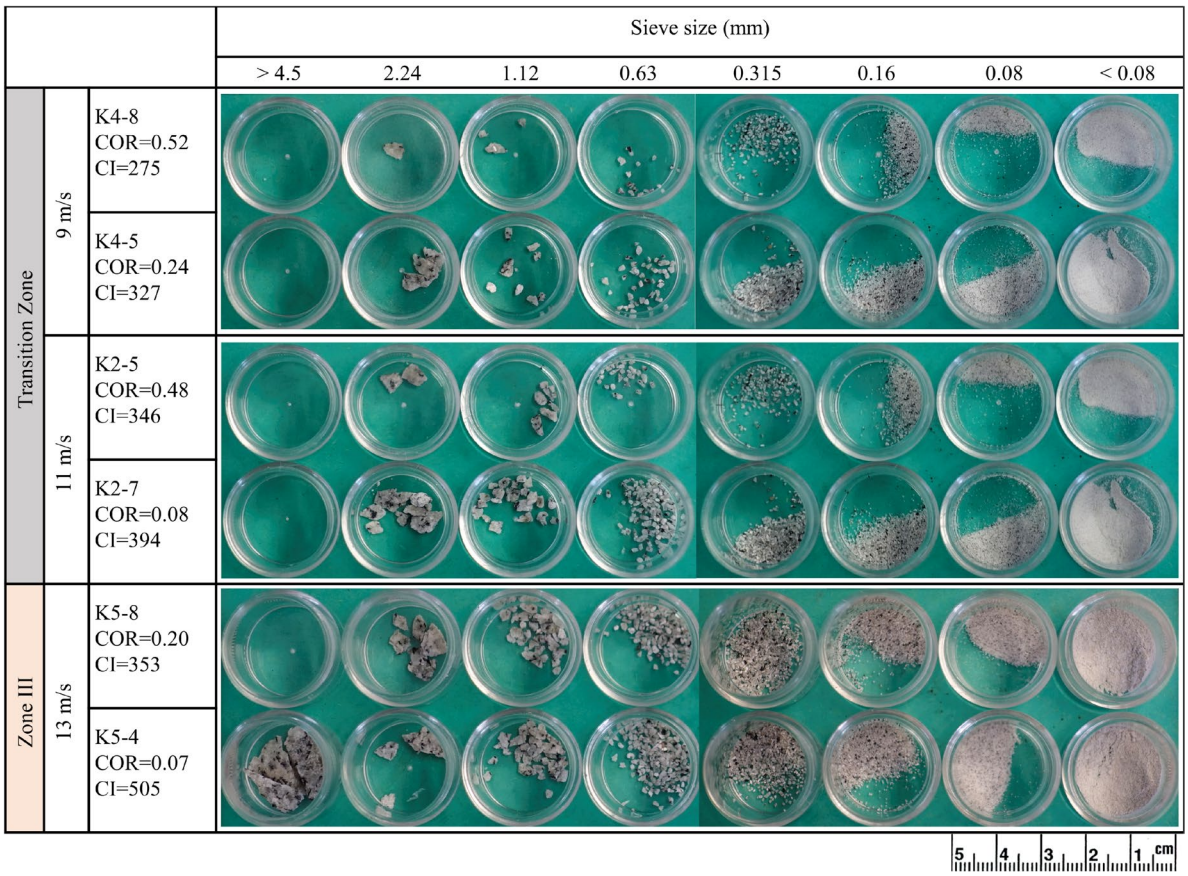

Fig. 18 Graphic comparison of the fragment size distribution of granite samples in the transition zone and zone III. It is observed that in samples with low COR, given the same impact speed, coarser fragments were created

variations in trends and their potential correlation with the COR.

In general, it can be observed that for impact velocities under v_2, all damage measurements exhibit a linear behavior relative to the impact velocity. This region is characterized by a relatively small dispersion and lower crater mass. Interestingly, in the case of the sandstone, even if the bit penetrates the rock more than 1 mm, only a plastic deformation was observed, and consequently no crater mass could be measured (see Fig. 19i). Above v_2, the linear trend breaks. The bit penetration and crater mass increase abruptly. This can be clearly observed in the graphs corresponding to the granite (Fig. 19b, e, h), where a jump in the bit penetration from approximately 0.8–2.0 mm correlates, on average, with a jump in the crater mass in the range of from 0.2 to 1.25 g. Notably, this jump is highly correlated with the discontinuity in the COR, accentuating the notion that the COR curves can contribute to the definition of an optimal operational point. From the upper limit of v_2, where the transition in the COR curve ends, a linear trend with low dispersion resumes. In terms of impact energy, the new slope is equal to the slope before the discontinuity, giving to the curves a staircase shape.

Regarding the raw penetration value in relation to the different piston ratios, it is clear that for the same piston speed, pistons #4 and # 5, both with r_m equal to one, achieve greater penetration compared to the lighter piston # 2, coinciding with the experiments reported by Karlsson et al. (1989) and the simulations performed by Lundberg (1985). However, in terms of impact energy, such advantage disappears. Indeed, when comparing penetration and mass removed in terms of energy, all three mass and length configurations are equivalent (see Figs. 19a, d and 19b, e). According to this, the graphs in the following sections are presented only as a function of impact energy. In Fig. 19g–i—crater mass versus impact energy—a dotted line has been included at the equivalent impact energy of v_1 to highlight the region where no fragment detachment occurred from the rock surface. This indicates the minimum energy value required to initiate fragment detachment. It is often noted that this point is actually a combination of dynamic force (impact velocity, and hence energy) and penetration that must be satisfied simultaneously

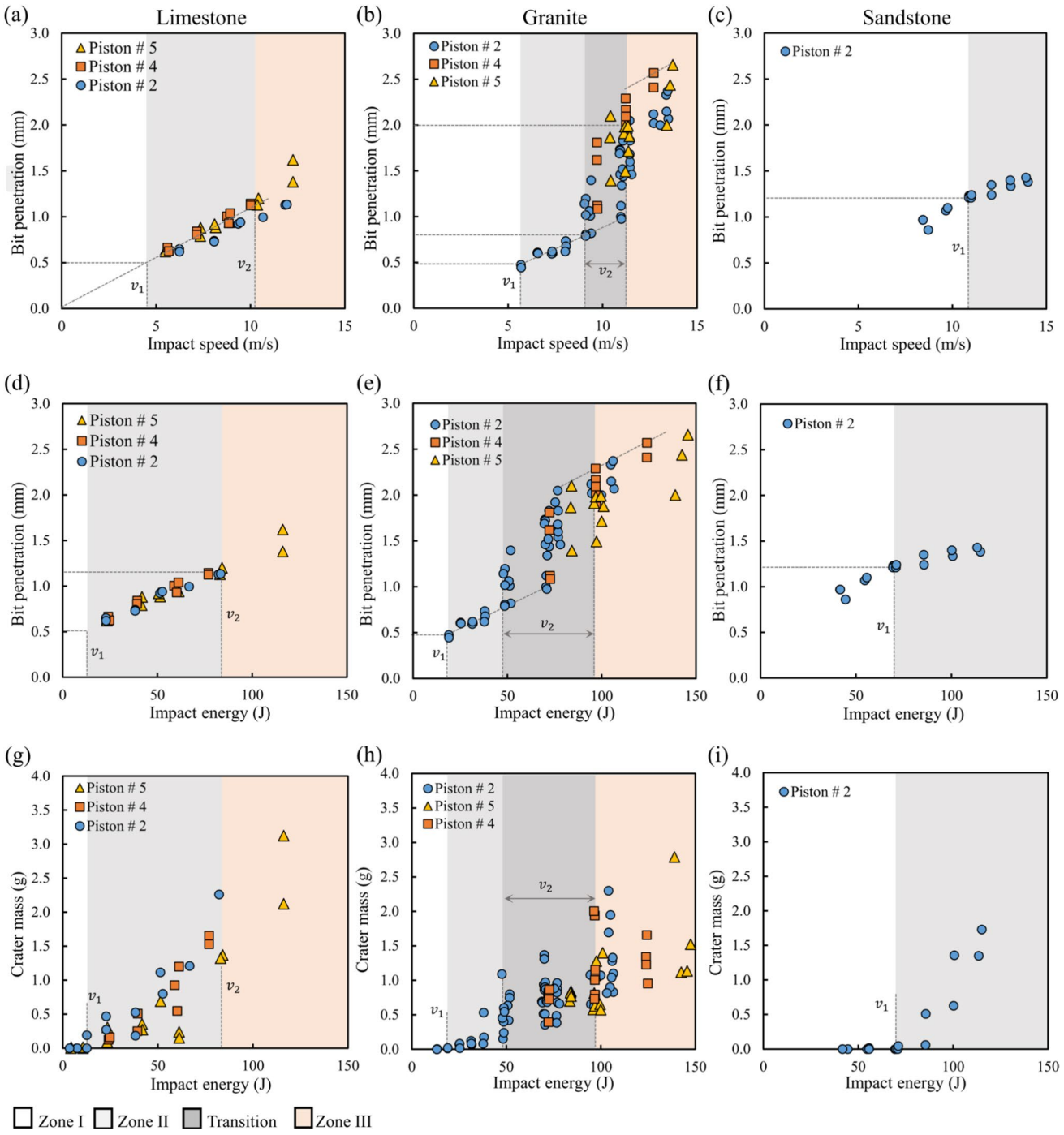

Fig. 19 Bit penetration as a function of the impact speed (1st row) and the impact energy (2nd row). Crater mass as a function of the impact energy (3rd row). Column A: limestone. Column B: granite. Column C: sandstone

(Wijk 1989). For the limestone, this point corresponds to an energy of 12.6 J, while a minimum penetration of 0.5 mm is required for the granite, the energy requirement is 19 J per insert with an indentation of 0.5 mm. In the case of the sandstone, these values are significantly higher, with fragmentation starting somewhere between 70 and 85 J per insert, and a minimum penetration of 1.2 mm. Considering that the typical impact energy per insert in a percussive rock drill falls within the range of 50–75 J, Rhune sandstone should be categorized as less drillable by percussive tools.

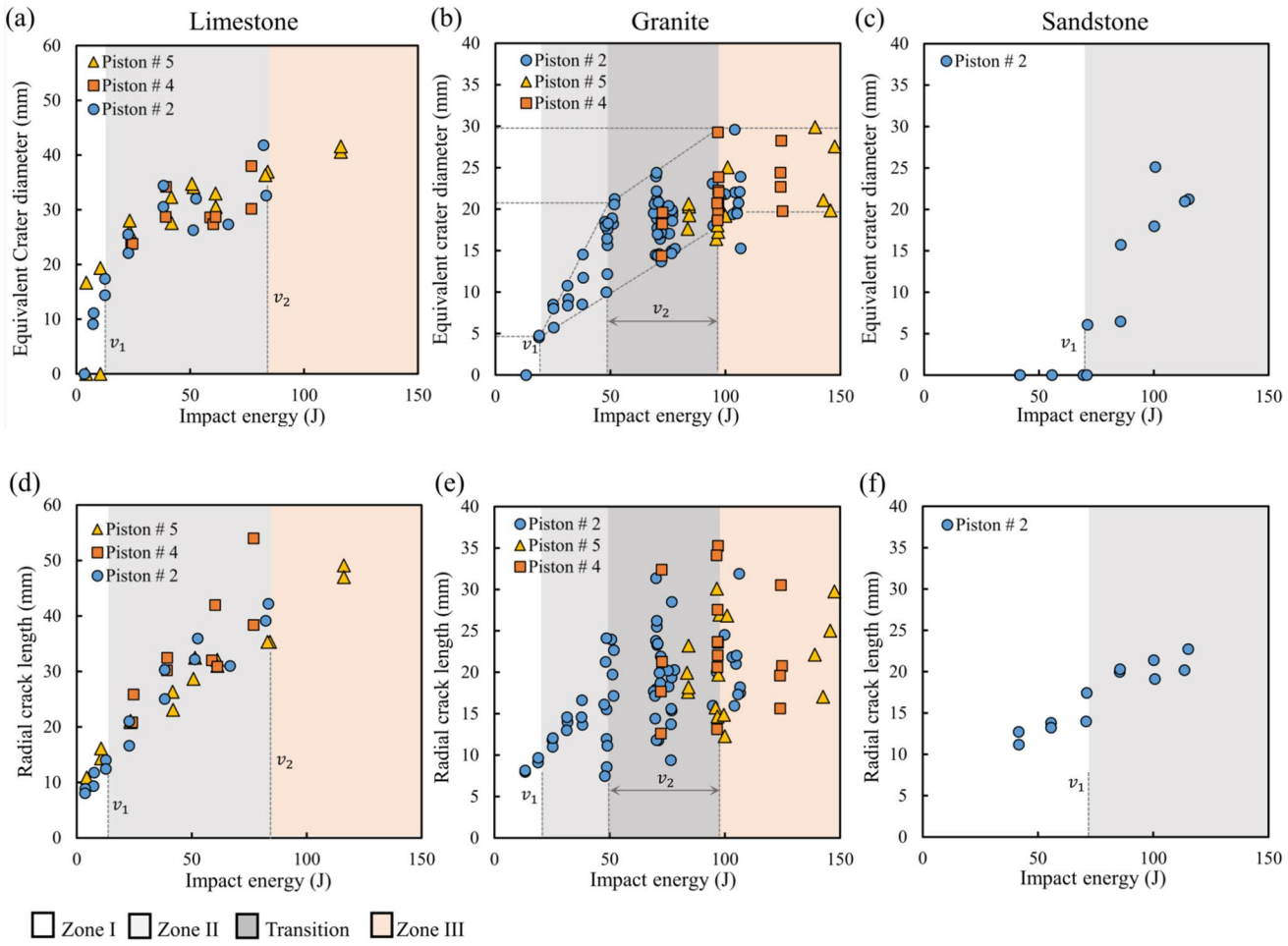

Fig. 20 Equivalent crater diameter and radial crack length as a function of the impact energy. Column A: limestone. Column B: granite. Column C: sandstone

4.5 Crater Dimensions

In this section, the equivalent crater diameter and the maximum radial crack length are analyzed as described in Sect. 3.2. Both variables have direct influence on the performance of percussive drilling tools, as both together define the rock surface state before a subsequent impacts occurs. Thus, they are critical in defining the optimum distance between neighboring inserts (Liu et al. 2008; Kim et al. 2020; Li et al. 2021). The relevant results are presented in Fig. 20. In granite (Fig. 20b, e), as the impact energy systematically increases, both the equivalent crater diameter and the length of radial cracks increase linearly up to approximately 50 J. From 50 J to approximately 100 J, the equivalent crater diameter slightly increases relative to the impact energy. Then, from 100 J, the growth rate becomes almost zero (Fig. 20b). As explained in Sect. 4.2, the physical explanation for these changes is related to the crushed zone and the side cracks (see Fig. 16 and its interpretation). Regarding the radial cracks (Fig. 20e), it can be observed that their extension becomes highly random beyond the transition zone: given that radial cracks in crystalline materials are generated in the loading phase due to tangential stresses (Cook and Pharr 1990; Saksala 2011), the random pulverization of the crushed zone—which acts as a physical medium to exert force from the bit to the undamaged part of the rock—acts as a stress relief, attenuating or preventing further radial crack propagation. A similar interpretation can be inferred from the probabilistic method proposed by Forquin and Hild (2010).

In the case of limestone (Fig. 20a, d), the equivalent crater diameter exhibits a non-linear behavior characterized by a region between 30 and 60 J where the growth rate is zero (Fig. 20a). Such staircase shapes related to the evolution of damage in rocks have been reported by Kou et al. (1977) and Souissi et al. (2015), studied numerically by Liu et al. (2008), and explained for Saint Anne limestone through XTC analyses by Aising et al. (2024a). Regarding the size of the radial cracks, we observed a linear trend

over the range of impact energies tested, because the contact between the bit and the rock was preserved, sometimes even in cases of fragmentation (see the central permanent deformation in Fig. 9b).

In the case of sandstone (Fig. 20c,f), it is interesting to note that although the lateral cracks were fully developed at impacts energies lower than 70 J (i.e., under v_1), and were of the same order of magnitude as in granite and limestone, fragmentation does not occur. For radial cracks (Fig. 20f), they present a linear relationship with respect to impact energy. Note that, as in the case of the limestone, Rhune sandstone also preserves the plastically deformed zone under contact with the insert (Fig. 9c).

5 Conclusions

In this study, we investigated the influence of different pistons to bit mass and length ratios on the piston coefficient of restitution COR in pristine rocks. Developing and using an experimental setup equipped with a high-speed camera, we observed the piston–bit–rock interaction throughout the impact process. The displacement curves of the piston and the bit were determined by tracking their ends from the videos. The analysis of these curves has revealed that, given the same impact velocity, higher or lower COR values can be obtained depending on the bit speed in the unloading phase and the conditionality of a second interaction with the piston.

For each of the three rocks tested, a characteristic COR curve was obtained as a function of the impact velocity. We discovered a non-linearity in the COR curve at a specific impact speed, which delineate regions of high and low COR. Remarkably, this non-linearity was independent of the piston-to-bit relationships, although it was specifically observed in limestone and granite. We presume that a similar threshold must exist for the sandstone tested, albeit at an impact velocity outside the range relevant to DTH hammers.

In the case of the granite, by using XCT, we investigated the persistence or absence of the fragmented zone after the impact. We found that when a low COR was measured, the plastically deformed and crushed zone was pulverized during the loading stroke of the bit, rendering the rock incapable of exerting any mechanical work on the bit due to elastic recovery. Sieving the fragments further demonstrated that a low COR corresponded to a coarser fragment distribution, a desirable characteristic for roto-percussive drilling tools. Additionally, we established that variables related to crater extension are primarily linked to the length of side cracks and the depth at which they nucleate. We showed a direct correlation between the length of a side crack and its nucleation depth.

Crater damage variables were measured using various techniques to identify potential correlations with the COR curves. We found that, under the same impact energy, the tested piston-to-bit mass and length ratios—which adequately covered those of commercial DTH hammers—have a minimal effect on each of the damage measurements made, with any difference attributed to the rock heterogeneity. This finding is particularly relevant to the industry, as it reveals that the impact energy is the only parameter determining the magnitude of the damage, independent of piston mass, piston length or impact velocity.

Finally, we observed that each turning point near the discontinuity in the COR curves correlated directly with changes in the growth rate of the damage descriptors, indicating that by measuring the COR while drilling, an optimal hammer operational point can be identified. Determining which of these turning points is optimal, or whether they will be exactly the same in real drilling operations, was beyond the scope of this research; therefore, field tests with hammers operating near these points must be conducted to elucidate this finding.

Future work will include further experimental testing to characterize the effect on COR curves of multiple impacts on pre-damaged rock, as well as testing real-scale hammers.

Acknowledgements We gratefully acknowledge the financial support provided by Drillco Tools S.A. We also extend our thanks to the technicians at ARMINES for their assistance in commissioning the experimental setup. Additionally, we appreciate the contributions of Delphine Gomez and Fabrice Echevarria from Cetim Sud-Ouest laboratory for their work in digitizing the rock samples.

Author Contributions The authors confirm their contribution to the paper as follows: JA: conceptualization, methodology, investigation, formal analysis, visualization, writing—original draft preparation. LG, HS: supervision, methodology, writing—review and editing. PS, PM: X-ray computed tomography acquisitions, 3D image reconstruction, writing and review.

Funding Open access funding provided by Mines Paris - PSL. This work is part of a PhD study funded by Drillco Tools S.A. and Mines Paris PSL.

Data Availability The authors declare that data supporting the findings of this study are available within the article.

Declarations

Conflict of interest The authors declare that they have no conflict of interest.

References

Aising J, Gerbaud L, Sellami H et al (2024a) Chipping mechanisms in rotary-percussive drilling: experimental insights into the role of the median crack as precursor of the dynamic fragmentation process. In: 58th U.S. Rock Mechanics/Geomechanics Symposium. ARMA

Aising J, Gerbaud L, Sellami H (2024b) Experimental analysis of rock fragmentation induced by single percussive impact. Int J Rock Mech Min Sci 181:105843. https://doi.org/10.1016/j.ijrmms.2024.105843

Aldannawy H, Rouabhi A, Gerbaud L (2022) Percussive drilling: experimental and numerical investigations. Rock Mech Rock Eng 55:1555–1570. https://doi.org/10.1007/s00603-021-02707-5

Aldannawy HA, Gerbaud L, Rouabhi A (2021) On the influence of tool shape on percussive drilling in hard rocks. In: 55th US Rock Mech/Geomech Symp 2021, vol 1, pp 517–526

Altindağ R (2003) Estimation of penetration rate in percussive drilling by means of coarseness index and mean particle size. Rock Mech Rock Eng 36:323–332. https://doi.org/10.1007/s00603-003-0002-3

Bu C, Qu Y, Cheng Z, Liu B (2009) Numerical simulation of impact on pneumatic DTH hammer percussive drilling. J Earth Sci 20:868–878. https://doi.org/10.1007/s12583-009-0073-5

Cazenave F, Gerbaud L, Sellami H et al (2021) ORCHYD_DeliverableD2.1

Changming W (1991) An analytical study of percussive energy transfer in hydraulic rock drills. Min Sci Technol 13:57–68. https://doi.org/10.1016/0167-9031(91)90254-A

Chiang LE, Elías DA (2008) A 3D FEM methodology for simulating the impact in rock-drilling hammers. Int J Rock Mech Min Sci 45:701–711. https://doi.org/10.1016/j.ijrmms.2007.08.001

Cnudde V, Boone MN (2013) High-resolution X-ray computed tomography in geosciences: a review of the current technology and applications. Earth-Sci Rev 123:1–17. https://doi.org/10.1016/j.earscirev.2013.04.003

Cook RF, Pharr GM (1990) Direct observation and analysis of indentation cracking in glasses and ceramics. J Am Ceram Soc 73:787–817. https://doi.org/10.1111/j.1151-2916.1990.tb05119.x

Depouhon A, Denoël V, Detournay E (2015) Numerical simulation of percussive drilling. Int J Numer Anal Methods Geomech 39:889–912. https://doi.org/10.1002/nag.2344

Dumoulin S, Thenevin I, Kane A et al (2024) A complete experimental study on hard granites: microstructural characterization, mechanical response, and failure criterion. Geomech Energy Environ. https://doi.org/10.1016/j.gete.2024.100592

Forquin P, Hild F (2010) A probabilistic damage model of the dynamic fragmentation process in brittle materials. Elsevier, Oxford

Fourmeau M, Kane A, Hokka M (2017) Experimental and numerical study of drill bit drop tests on Kuru granite. Philos Trans R Soc A Math Phys Eng Sci. https://doi.org/10.1098/rsta.2016.0176

Gilardi G, Sharf I (2002) Literature survey of contact dynamics modelling. Mech Mach Theory 37:1213–1239. https://doi.org/10.1016/S0094-114X(02)00045-9

Gilbert Y, Hagström M (2010) Getliff JM (2010) Reducing the carbon footprint of drilling and completion operations. Soc Pet Eng SPE Int Conf Heal Saf Environ Oil Gas Explor Prod 2:1280–1294. https://doi.org/10.2118/126756-ms

Goldsmith W (1960) Impact: the theory and physical behavior of colliding solids. Edward Arnold Publishers, London

Hartman HL (1963) The simulation of percussion drilling in the laboratory by indexed-blow studies. Soc Pet Eng J 3:214–226. https://doi.org/10.2118/500-pa

Izquierdo LE, Chiang LE (2004) A methodology for estimation of the specific rock energy index using corrected down-the-hole drill monitoring data. Inst Min Metall Trans Sect A Min Technol 113:225–236. https://doi.org/10.1179/037178404225006218

Jiang H, Cai Z, Wang O, Meng D (2020) Experimental and numerical investigation of hard rock breakage by indenter impact. Shock Vib. https://doi.org/10.1155/2020/2747830

Karlsson LG, Lundberg B, Sundin KG (1989) Experimental study of a percussive process for rock fragmentation. Int J Rock Mech Min Sci 26:45–50. https://doi.org/10.1016/0148-9062(89)90524-X

Karpov VN, Timonin VV (2018) Importance of early adjustment of rotary-percussion drilling tool to mineral mining conditions. In: IOP conference series: earth and environmental science

Kazhdan M, Bolitho M, Hoppe H (2006) Poisson surface reconstruction. In: Eurographics symposium on geometry processing, pp 61–70

Kim DJ, Kim J, Lee B et al (2020) Prediction model of drilling performance for percussive rock drilling tool. Adv Civ Eng. https://doi.org/10.1155/2020/8865684

Kou SQ, Xiangchun T, Lindqvist PA (1977) Modelling of excavation depth and fractures in rock caused by tool indentation

Kou SQ, Liu HY, Lindqvist P-A, Tang CA (2004) Rock fragmentation mechanisms induced by a drill bit. Int J Rock Mech Min Sci 41:460. https://doi.org/10.1016/j.ijrmms.2003.12.127

Kwon K, Song C, Park J et al (2013) Rock fragmentation assessment of a drill bit by hopkinson bar percussion test. J Korean Soc Rock Mech 23:42–53. https://doi.org/10.7474/tus.2013.23.1.042

Lawn B, Wilshaw R (1975) Indentation fracture: principles and applications. J Mater Sci 10:1049–1081

Li H, Liu S, Chang H (2020) Experimental research on the influence of working parameters on the drilling efficiency. Tunn Undergr Sp Technol 95:103174. https://doi.org/10.1016/j.tust.2019.103174

Li X, Rupert G, Summers DA et al (2000) Analysis of impact hammer rebound to estimate rock drillability. Rock Mech Rock Eng 33:1–13. https://doi.org/10.1007/s006030050001

Li Y, Peng J, Zhang P, Huang C (2021) Hard rock fragmentation in percussion drilling considering confining pressure: insights from an experimental study. Int J Rock Mech Min Sci 148:104961. https://doi.org/10.1016/j.ijrmms.2021.104961

Liu HY, Kou SQ, Lindqvist PA (2008) Numerical studies on bit-rock fragmentation mechanisms. Int J Geomech 8:45–67. https://doi.org/10.1061/(asce)1532-3641(2008)8:1(45)

Liu S, Chang H, Li H, Cheng G (2017) Numerical and experimental investigation of the impact fragmentation of bluestone using multi-type bits. Int J Rock Mech Min Sci 91:18–28. https://doi.org/10.1016/j.ijrmms.2016.11.006

Lückemann P, Forrester S, Mears A et al (2020) Assessment of measurement uncertainty in optical marker tracking of high-speed motion. https://doi.org/10.3390/proceedings2020049072

Lundberg B (1973) Energy transfer in percussive rock destruction-II. Supplement on hammer drilling. Int J Rock Mech Min Sci 10:401–419. https://doi.org/10.1016/0148-9062(73)90025-9

Lundberg B (1985) Microcomputer simulation of percussive drilling. Int J Rock Mech Min Sci 22:237–249. https://doi.org/10.1016/0148-9062(85)92951-1

Lundberg B, Collet P (2010) Optimal wave with respect to efficiency in percussive drilling with integral drill steel. Int J Impact Eng 37:901–906. https://doi.org/10.1016/j.ijimpeng.2010.02.001

Lundberg B, Collet P (2015) Optimal wave shape with respect to efficiency in percussive drilling with detachable drill bit. Int J Impact Eng 86:179–187. https://doi.org/10.1016/j.ijimpeng.2015.06.021

Lundberg B, Huo J (2017) Biconvex versus bilinear force-penetration relationship in percussive drilling of rock. Int J Impact Eng 100:7–12. https://doi.org/10.1016/j.ijimpeng.2016.10.002

Lundberg B, Rastemo T, Huo J (2021) Effect of pre-impact waves in an elastic rod on coefficient of restitution. Int J Impact Eng 151:103816. https://doi.org/10.1016/j.ijimpeng.2021.103816

Ma Y, Gong Q, Zhou X et al (2023) The modelling of rock fragmentation mechanisms by carbide buttons using the 3D discrete element method. Appl Sci. https://doi.org/10.3390/app13106090

Mardoukhi A, Hokka M, Kuokkala V (2018) Experimental study of the dynamic indentation damage in thermally shocked granite. Raken Mek 51:10–26. https://doi.org/10.23998/rm.69036

Mo P, Li Y (2019) Estimating the three-dimensional joint roughness coefficient value of rock fractures. Bull Eng Geol Environ 78:857–866. https://doi.org/10.1007/s10064-017-1150-0

Reyes et al (2015) Cuttings analysis for rotary drilling penetration mechanisms and performance evaluation. In: 49th US Rock mechanics/geomechanics symposium, pp 1498–1505

Saadati M, Forquin P, Weddfelt K, Larsson PL (2013) Granite rock fragmentation at percussive drilling. In: Rock dynamics and applications—state of the art, pp 437–442

Saksala T (2011) Numerical modelling of bit–rock fracture mechanisms in percussive drilling with a continuum approach. Int J Numer Anal Methods Geomech 30:1483–1505. https://doi.org/10.1002/nag.974

Saksala T, Gomon D, Hokka M, Kuokkala VT (2014) Numerical and experimental study of percussive drilling with a triple-button bit on Kuru granite. Int J Impact Eng 72:56–66. https://doi.org/10.1016/j.ijimpeng.2014.05.006

Saur H, Moonen P, Aubourg C (2021) Grain fabric heterogeneity in strained shales: insights from XCT measurements. J Geophys Res Solid Earth 126:1–19. https://doi.org/10.1029/2021JB022025

Saur H, Sénéchal P, Boiron T et al (2020) First investigation of quartz and calcite shape fabrics in strained shales by means of X-ray tomography. J Struct Geol. https://doi.org/10.1016/j.jsg.2019.103905

Song C, Chung J, Cho JS, Nam YJ (2018) Optimal design parameters of a percussive drilling system for efficiency improvement. Adv Mater Sci Eng. https://doi.org/10.1155/2018/2346598

Song H, Shi H, Yuan G et al (2022) Experimental study of the energy transfer efficiency and rock fragmentation characteristics in percussive drilling. Geothermics 105:102497. https://doi.org/10.1016/j.geothermics.2022.102497

Souissi S, Hamdi E, Sellami H (2015) Microstructure effect on hard rock damage and fracture during indentation process. Geotech Geol Eng 33:1539–1550. https://doi.org/10.1007/s10706-015-9920-6

Teale R (1965) The concept of specific energy in rock drilling. Int J Rock Mech Min Sci 2:57–73. https://doi.org/10.1016/0148-9062(65)90022-7

Ulusay R (ed) (2015) The ISRM suggested methods for rock characterization, testing and monitoring, 2007–2014

Wijk G (1989) The stamp test for rock drillability classification. Int J Rock Mech Min Sci 26:37–44. https://doi.org/10.1016/0148-9062(89)90523-8

Yang Y, Liao H, Xu Y et al (2019) Theoretical investigation of the energy transfer efficiency under percussive drilling loads. Arab J Geosci. https://doi.org/10.1007/s12517-019-4361-9

Zhang ZX (2004) Estimate of loading rate for a TBM machine based on measured cutter forces. Rock Mech Rock Eng 37:239–248. https://doi.org/10.1007/s00603-004-0025-4

Zhang T, Yu L, Peng Y et al (2023) Effect of the mineral spatial distribution heterogeneity on the tensile strength of granite: Insights from PFC3D-GBM numerical analysis. J Rock Mech Geotech Eng 15:1144–1160. https://doi.org/10.1016/j.jrmge.2022.07.012